Title
Decay Branching Ratios of Excited States in Mg24

Author
Munson, Justin Michael

Publication Date
2015

Peer reviewed|Thesis/dissertation

Decay Branching Ratios of Excited States in Mg24

by

Justin Michael Munson

A dissertation submitted in partial satisfaction of the
requirements for the degree of
Doctor of Philosophy

in

Engineering - Nuclear Engineering

in the

Graduate Division

of the

University of California, Berkeley

Committee in charge:

Dr. Eric Norman, Chair
Dr. Kai Vetter
Dr. Larry Phair
Dr. Daniel Kasen

Summer 2015

Decay Branching Ratios of Excited States in Mg24

Abstract

Decay Branching Ratios of Excited States in Mg24

by

Justin Michael Munson

Doctor of Philosophy in Engineering - Nuclear Engineering

University of California, Berkeley

Dr. Eric Norman, Chair

The carbon burning nuclear reactions ^{12}C(^{12}C, α)^{20}Ne, ^{12}C(^{12}C, p)^{23}Na, and ^{12}C(^{12}C, n)^{23}Mg occur during the carbon burning phase of sufficiently large stars and during explosive events such as supernovae. The Gamow window for these reactions is typically around 1.5 MeV, however direct measurements at energies in this range are very difficult due to the large Coulomb barrier between the carbon atoms. The compound nucleus formed during these reactions is ^{24}Mg. For energies around the Gamow window this compound nucleus has an excitation energy of 15 to 16 MeV. A surrogate experiment which produces the compound nucleus can measure the branching ratios for the excited compound nucleus and thus the ratios between the carbon burning reaction cross sections. An experiment was performed using inelastic scattering of 40 MeV alpha particles to produce ^{24}Mg excited up to 27 MeV and the applicability of these results as a surrogate for the carbon burning reactions is examined. A successful surrogate measurement, which this experiment partially achieves, will both provide the branching ratios within the Gamow window and aid future direct measurements of carbon burning within the Gamow window.

Contents

List of Figures

List of Tables

Acknowledgments

I would like to thank Eric Norman as my adviser at UC-Berkeley, Jason Burke as my primary contact at LLNL and the lead for the STARS-LiBerACE, STARLiTe, and STAR-LiTeR group that made this measurement possible, Larry Phair for his help particularly in the setup and test run phases at the LBNL 88" Cyclotron and Daniel Lee for the production of the magnesium targets. I would like to thank Robert Casperson, Ellen McCleskey, Matt McCleskey, Richard Hughes, and Shuya Ota for their help in setting up, troubleshooting, and taking shifts both before and during the runs. I would also like to thank Shamsuzzoha Basunia, Jennifer Jo Ressler, Perry Chodash, Agnieszka Czeszumska, Roby Austin, Antti Saastamoinen, Alex Spiridon, Roman Chyzh, and Timothy Ross for taking shifts on the experiment, often at late hours, and for the staff at both the LBNL 88" Cyclotron and the Texas A&M Cyclotron Institute, both for their work providing the beam and for the help received from the machine shop staff at each facility.

Without their assistance as well as that of others I've failed to list this project could not have been completed. Thank you.

Chapter 1

Introduction

The decay branching ratios of ^{24}Mg inelastically excited to energies up to 27 MeV were measured. In addition to providing data on inelastic scattering itself, this measurement was selected to gain knowledge about stellar carbon burning. During carbon burning in stars, carbon undergoes the reactions $^{12}\mathrm{C} + ^{12}\mathrm{C} \rightarrow ^{20}\mathrm{Ne} + \alpha$, $^{12}\mathrm{C} + ^{12}\mathrm{C} \rightarrow ^{23}\mathrm{Na} + \mathrm{p}$, and $^{12}\mathrm{C} + ^{12}\mathrm{C} \rightarrow ^{23}\mathrm{Mg} + \mathrm{n}$. These reactions proceed through a short lived compound nucleus of excited ^{24}Mg. At a typical carbon burning temperature of $5 * 10^8$ K the reactions take place at a center of mass energy of 1 to 2 MeV, corresponding to an excitation energy in the ^{24}Mg nucleus of 15 to 16 MeV.

With the compound nucleus assumption the cross section for each reaction is the product of the formation cross section for the compound nucleus and the branching ratio for the compound nucleus to decay by the corresponding exit channel. Since the ^{24}Mg compound nucleus is formed with a high level of excitation, many overlapping states in the compound nucleus contribute. The formation cross section for a given energy window is the sum of the formation cross sections for each underlying state and the branching ratio is a weighted average of the branching ratios of the populated compound nucleus states. In particular, there will be a distribution of excited states in the compound nuclei with regard to energy, spin, and parity.

The surrogate method is an approach to studying cross sections that makes use of the compound nucleus assumption. Since the branching ratios are a function of the compound nucleus, the same compound nucleus produced by a different formation reaction will still have the same branching ratios. However, since different formation cross sections may produce compound nuclei with different spin and parity distributions, assumptions must often be made about how the surrogate compound nucleus compares to the desired compound nucleus. One common assumption is the Weisskopf-Ewing limit which states that under certain conditions the branching ratios for the compound nucleus do not depend on spin or parity. This is discussed more in Chapter 3.

The surrogate method is used to measure cross sections for reactions that are impractical to measure directly. In the case of carbon burning the formation cross section for two ^{12}C

nuclei to form a ^{24}Mg compound nucleus falls off rapidly with decreasing energy due to the Coulomb barrier between the carbon nuclei. Direct measurements for carbon burning have been made down to around 2 to 2.5 MeV [1] [2] [3] [4] [5] [6] [7]. This is still higher than the 1 to 2 MeV energies of primary interest to stellar carbon burning.

This work presents measurements of the branching ratios of ^{24}Mg inelastically excited by 40 MeV alpha particles and discusses the application of these measurements as a surrogate for carbon burning. Chapter 2 gives an overview of the astrophysical motivation to study carbon burning and existing measurements for these reactions. Chapter 3 discusses the surrogate method. Chapter 4 details the experiments performed and the equipment used. Chapter 5 describes the analysis methods used and discusses the results obtained. Chapter 6 gives the conclusions reached.

Chapter 2

Astrophysical Motivation

2.1 Stellar Evolution

To introduce the importance of carbon burning in stars a brief overview of the lifecycle of a star is presented. Texts such as [8] and [9] give a more detailed treatment. This overview is primarily drawn from these two sources.

The evolution of a star is a sequence of gravitational contraction and nuclear reaction phases[8]. When a cloud of gas contracts the gravitational potential energy released provides a source of thermal energy which allows the ignition of the first nuclear burning phase, hydrogen burning. Hydrogen burning can follow the p-p chain, one of the CNO cycles (I-IV, or at higher temperatures the "Hot CNO" cycle), the NeNa cycle, or the MgAl cycle. The p-p chain reactions are listed in Table 2.1 and the CNO cycle reactions are listed in Table 2.2. Which reaction is dominant depends on the temperature of the star. The sun generates about 10% of its energy from the CNO cycle, though at core temperatures slightly higher than the sun the CNO cycle will dominate[9]. The CNO cycle also requires the presence of carbon, nitrogen, and oxygen catalysts that are not present in first generation stars, limiting these stars to the proton-proton chains.

Hydrogen burning provides pressure in stars that prevents further gravitational contraction. Since this is the longest burn phase, stars in their hydrogen burning phase are referred to as main sequence stars[8]. Higher mass stars have higher luminosity since more pressure from the burn is required to find equilibrium. As a result, higher mass stars exhaust their hydrogen fuel in less time than lower mass stars. As the hydrogen fuel is exhausted, gravitational contraction again takes over until the temperatures needed for helium burning are reached. In the process, the gravitational contraction will accelerate the hydrogen burning near the core, driving the outer layer away from the core to form a red giant[8].

Helium burning proceeds by the triple alpha process. This process can be thought of as two reactions. The first is $^4\mathrm{He} + ^4\mathrm{He} \leftrightarrow ^8\mathrm{Be}$. The isotope ^{8}Be has a very short (10^{-16} seconds) lifetime and so to have a significant population of ^{8}Be the temperature needs to

	$^{1}\mathrm{H} + ^{1}\mathrm{H}$	$\rightarrow$	$^{2}\mathrm{H} + \mathrm{e}^{+} + \nu_{\mathrm{e}}$
PP-I	$^{2}\mathrm{H} + ^{1}\mathrm{H}$	$\rightarrow$	$^{3}\mathrm{He} + \gamma$
	$^{3}\mathrm{He} + ^{3}\mathrm{He}$	$\rightarrow$	$^{4}\mathrm{He} + ^{1}\mathrm{H} + ^{1}\mathrm{H}$
	$^{3}\mathrm{He} + ^{4}\mathrm{He}$	$\rightarrow$	$^{7}\mathrm{Be} + \gamma$
PP-II	$^{7}\mathrm{Be} + \mathrm{e}^{-}$	$\rightarrow$	$^{7}\mathrm{Li} + \nu_{\mathrm{e}}(+\gamma)$
	$^{7}\mathrm{Li} + ^{1}\mathrm{H}$	$\rightarrow$	$^{4}\mathrm{He} + ^{4}\mathrm{He}$
	$^{7}\mathrm{Be} + ^{1}\mathrm{H}$	$\rightarrow$	$^{8}\mathrm{Be} + \gamma$
PP-III	$^{8}\mathrm{B}$	$\rightarrow$	$^{8}\mathrm{Be} + \mathrm{e}^{+} + \nu_{\mathrm{e}}$
	$^{8}\mathrm{Be}$	$\rightarrow$	$^{4}\mathrm{He} + ^{4}\mathrm{He}$

Table 2.1: Proton-proton reaction chains. The PP-II chain is an alternative to the third reaction listed for PP-I, and the PP-III chain is an alternative to the second reaction listed for PP-II. Table contents are taken from [9].

	$^{12}\mathrm{C} + ^{1}\mathrm{H}$	$\rightarrow$	$^{13}\mathrm{N} + \gamma$
	$^{13}\mathrm{N}$	$\rightarrow$	$^{13}\mathrm{C} + \mathrm{e}^{+} + \nu_{\mathrm{e}}$
CNO-I	$^{13}\mathrm{C} + ^{1}\mathrm{H}$	$\rightarrow$	$^{14}\mathrm{N} + \gamma$
(CN)	$^{14}\mathrm{N} + ^{1}\mathrm{H}$	$\rightarrow$	$^{15}\mathrm{O} + \gamma$
	$^{15}\mathrm{O}$	$\rightarrow$	$^{15}\mathrm{N} + \mathrm{e}^{+} + \nu_{\mathrm{e}}$
	$^{15}\mathrm{N} + ^{1}\mathrm{H}$	$\rightarrow$	$^{12}\mathrm{C} + ^{4}\mathrm{He}$
	$^{15}\mathrm{N} + ^{1}\mathrm{H}$	$\rightarrow$	$^{16}\mathrm{O} + \gamma$
CNO-II	$^{16}\mathrm{O} + ^{1}\mathrm{H}$	$\rightarrow$	$^{17}\mathrm{F} + \gamma$
	$^{17}\mathrm{F}$	$\rightarrow$	$^{17}\mathrm{O} + \mathrm{e}^{+} + \nu_{\mathrm{e}}$
	$^{17}\mathrm{O} + ^{1}\mathrm{H}$	$\rightarrow$	$^{14}\mathrm{N} + ^{4}\mathrm{He}$
	$^{17}\mathrm{O} + ^{1}\mathrm{H}$	$\rightarrow$	$^{18}\mathrm{F} + \gamma$
CNO-III	$^{18}\mathrm{F}$	$\rightarrow$	$^{18}\mathrm{O} + \mathrm{e}^{+} + \nu$
	$^{18}\mathrm{O} + ^{1}\mathrm{H}$	$\rightarrow$	$^{15}\mathrm{N} + ^{4}\mathrm{He}$
CNO-IV	$^{18}\mathrm{O} + ^{1}\mathrm{H}$	$\rightarrow$	$^{19}\mathrm{F} + \gamma$
	$^{19}\mathrm{F} + ^{1}\mathrm{H}$	$\rightarrow$	$^{16}\mathrm{O} + ^{4}\mathrm{He}$

Table 2.2: The CNO Cycles. Each higher numbered cycle begins as an alternative of the final listed reaction of the previous cycle and returns to a lower numbered cycle with the last listed reaction. Reactions are from [9] and [8].

reach a minimum of about $1.2 * 10^8$ Kelvin[9] where a significant population of ^{4}He can access the resonant reaction to the ground state of ^{8}Be. With a population of ^{8}Be formed the capture reaction ^{8}Be $+^4$ He $\leftrightarrow^{12}$ C can proceed. The carbon is formed in its 7.654 MeV excited state which has a high probability of emitting an alpha, so again a high production rate of the excited ^{12}C is needed so that the gamma decay channel can produce significant quantities of ground state ^{12}C[9].

Following helium burning, gravitational contraction can continue to begin carbon burning. In this process, two carbon nuclei are consumed, producing neon, sodium, or magnesium. The amount of each product is determined by the branching ratio of the nuclear reaction as well as by the total reaction rate. At stellar temperatures the total reaction rate is dominated by the Coulomb barrier[8][9]. Since the average kinetic energy of the carbon nuclei is well below the Coulomb barrier, the total cross section is very small, and rapidly decreases with decreasing energy. Attempts to measure the cross section using particle accelerators becomes increasingly difficult as the energy is decreased closer to those of astrophysical interest.

The Coulomb barrier is not as restrictive to the exit channels. The alpha and proton channels which produce neon and sodium are both exothermic [10] and release enough energy that even if the two carbon nuclei had zero kinetic energy, the alpha particle or proton would be above its Coulomb barrier. The neutron channel has no Coulomb barrier, but is slightly endothermic and only contributes at higher energies. In principle two carbon nuclei could also be emitted, however the same Coulomb barrier which dominates the total reaction rate makes this channel very small.

While any measurement of the entrance channel will have to contend with the $^{12}C +^{12} C$ Coulomb barrier in some manner, measuring the exit channels alone can avoid this difficulty. By recreating the nuclear conditions which occur after two carbon nuclei penetrate their mutual Coulomb barrier, the exit channels' branching ratios can be measured. By making some assumptions about the compound nucleus, primarily that the particles come to thermal equilibrium prior to particle emission, this becomes a realistic approach [11].

2.2 The Gamow Window

The nuclei within a star have a thermal distribution given by the Maxwell-Boltzmann velocity distribution

$$\phi(v) = 4\pi v^2 \left(\frac{m}{2\pi kT}\right)^{3/2} exp\left(-\frac{mv^2}{2kT}\right) \tag{2.1}$$

or in terms of energy as[8]

$$\phi(E) \propto E * exp(-E/kT) \tag{2.2}$$

At high energies ($E \gg kT$) the density decreases exponentially with increasing energy.

The nuclear reaction cross sections for charged particles at stellar energies are dominated by the probability of penetrating the Coulomb barrier. At energies well below the Coulomb barrier peak this penetration probability is approximated by

$$P = exp(-2\pi\eta) \tag{2.3}$$

where η is the Sommerfeld parameter $\eta = \frac{Z_1 Z_2 e^2}{\hbar v} = \frac{31.29}{2\pi} Z_1 Z_2 \left(\frac{\mu}{E}\right)^{1/2}$ [8]. It is common to express astrophysical cross sections in the form

$$\sigma(E) = \frac{1}{E} exp(-2\pi\eta) S(E) \tag{2.4}$$

where the $\frac{1}{E}$ term accounts for the energy dependence of the de Broglie wavelength ($\pi\lambda\!\!\!^{-2} \propto \frac{1}{E}$) which relates to the classical analog of the area of the target as seen by the projectile, and the term $S(E)$ contains the nuclear effects on the cross section. In the absence of resonances $S(E)$ is a slowly changing function of energy[8].

The reaction rate is a function of both the cross section at a given energy and the population of the reacting nuclei at that energy. Thus for a given temperature the (differential) reaction rate as a function of energy is of the form

$$\frac{dr}{dE} \propto \phi(E)\sigma(E) \tag{2.5}$$

where $\frac{dr}{dE}$ is the reaction rate at a given energy [8]. Entering the formulas for $\phi(E)$ and $\sigma(E)$ from above results in

$$\frac{dr}{dE} \propto E * exp(-E/kT) \frac{1}{E} exp(-2\pi\eta) S(E) = exp(-E/kT - 2\pi\eta) S(E) \tag{2.6}$$

The energy dependence of $2\pi\eta$ can be separated out,

$$2\pi\eta = \frac{b}{E^{1/2}} \tag{2.7}$$

where $b = (2\mu)^{1/2}\pi e^2 Z_1 Z_2/\hbar = 0.989 Z_1 Z_2 \mu^{1/2} (MeV)^{1/2}$. This defines the Gamow energy, which is b^2 [8].

Assuming that $S(E)$ is relatively constant, the reaction rate as a function of energy can be qualitatively described by

$$\frac{dr}{dE} \propto exp\left(-\frac{E}{kT} - \frac{b}{E^{1/2}}\right) \tag{2.8}$$

This is shown in Figure 2.1.

A feature of this function is a peak where most reactions occur. The energy range containing this peak is the Gamow window. At energies above the Gamow window the thermal population of nuclei is too small to have a significant contribution to the total

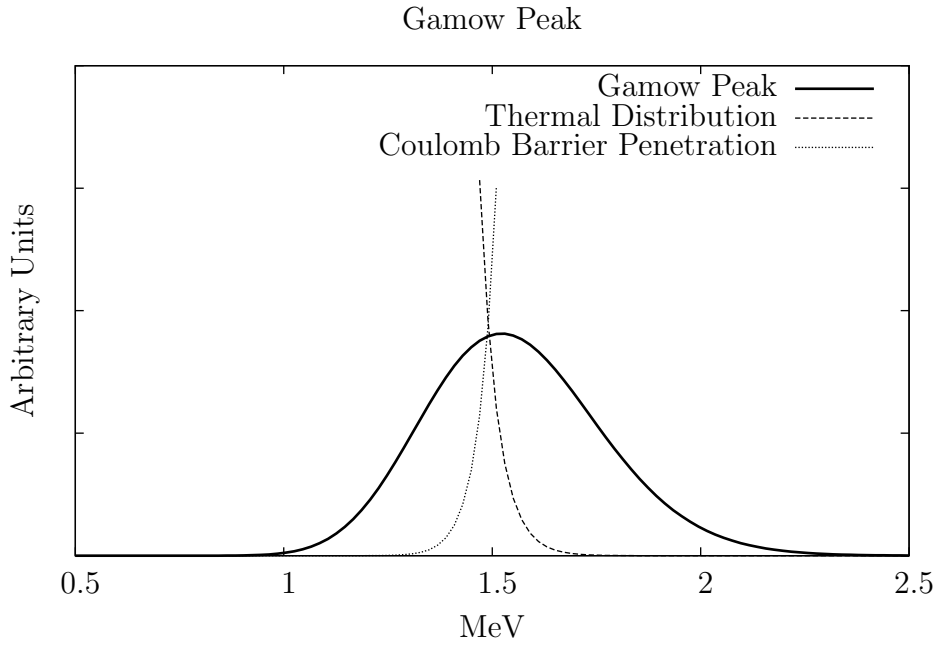

Figure 2.1: An approximation of the reaction rate as a function of energy for two ^{12}C nuclei at $5 * 10^8$ Kelvin. The units for the vertical axis are arbitrary. This is similar to a plot in [8].

reaction rate, and at energies below the Gamow window the cross section falls off too rapidly to have a significant contribution. As a result, cross section measurements are most useful and will have the greatest impact in the energy range of the Gamow window.

2.3 Steady Carbon Burning

In stars of greater mass than around 8-10 times that of the sun carbon burning can occur at a steady rate following the hydrogen and helium burning phases. For example a 25 solar mass star will undergo a steady carbon burning phase for around 600 years[8]. This process occurs at a temperature around $5 * 10^8$ K [8].

2.4 Supernovae

A bright nova was identified with the combination of the observation the nova on August 31, 1885 by Hartwig in the Andromeda galaxy and the estimation of the distance to Andromeda galaxy by Lundmark in 1920[12] [13]. The distinction between novae and supernovae was first made by Baade and Zwicky in 1934 [14] [13]. Initially the distinction between novae and supernovae was one of magnitude, with supernovae releasing on the order of 1000 times the energy of other novae. Novae are the result of mass transfer in a binary star system, eventually causing the transferred hydrogen to ignite, leading to a greatly increased brightness which fades over time. The two binary stars remain and the cycle can repeat [9]. Some but not all types of supernovae involve binary systems and the explosion in a supernova leads to a major change in the star itself, such as complete disruption, a remnant white dwarf, neutron star, or black hole [9]. The division of supernovae into types I and II was made in 1940 by Minkowski [15]. A further division of type I supernovae was made by Wheeler and Harkness [16] after studies going back as early as 1960 [17] [18] [19].

Type Ia supernovae have become of particular interest due to their use as distance indicators or standard candles. The idea that supernovae could be used to estimate distances to galaxies was proposed by both Zwicky in 1938 [20] and Wilson in 1939 [21] due to their relatively uniform brightness. Most of the supernovae which led to this conclusion were later determined to be of type Ia [13].

While type Ia supernovae do appear fairly uniform, they do exhibit enough variability that there may be differences among the source stars and the explosion mechanisms [13]. This leads to a desire for a well understood explosion model, hopefully leading to a greater confidence when using these supernovae to estimate distances.

Numerous models have been proposed for explaining in paticular type Ia supernovae. These models can be divided into Chandrasekhar mass explosion models, sub- chandrasekhar mass models and colliding white dwarf models. Chadrasekhar mass models can further be divided into deflagration, delayed detonation and pulsed detonation models [13] which differ

in the manner in which the reaction front travels through the star.

Chandrasekhar mass explosion models are based on a white dwarf star gaining material from a nearby companion star until it approaches the Chandrasekhar mass, the mass which can be supported by electron degeneracy. Such a star then begins to contract, converting gravitational energy into heat and igniting the primarily carbon fuel to create a supernova [17].

Soon after the distinction between novae and supernovae was made by Baade and Zwicky it was also recognized that supernovae were good candidates for producing heavy elements. An early model for this was that a statistical equilibrium would form in supernovae between radiation and radioactive nuclei [22]. For a density of 10^7 grams/cm and a temperature of $4 * 10^9$ kelvin this equilibrum is reached in about 100 seconds, with a strong dependence on temperature [22].

2.5 Previous Measurements

A number of direct measurements have been made by bombarding a ^{12}C target with a ^{12}C beam [1] [2] [3] [4] [5] [6] [7]. Many of these experiments measured the alpha, proton and neutron channels by detecting the emitted gamma rays from the resulting ^{20}Ne, ^{23}Na and ^{23}Mg nuclei [2] [4] [5] [6] [7]. This method only measures the reactions which produce an excited product nuclei. The portion of the reaction producing ground state nuclei must be added in by theory or by comparison to other experiments.

Some differences exist in the various data sets. The total fusion cross section differences are discussed and a potential resolution is presented by Aguilera et al. [5] who proposed a shift in the energy scale and a normalization factor be applied to each data set. These factors were justified by the possibility that carbon could build up on a target and compromise the energy measurement of outgoing particles as well as the measurement of the total number of target atoms. Since the total cross section is rapidly decreasing with decreasing energy, a small shift in the energy scale can result in a large change in the measured cross section. In the vicinity of 4.5 MeV, a 200 keV shift results in approximately a factor of 2 change in total cross section [5].

A few methods have been proposed to extend the total cross section measurements to lower energies. One method uses the generalized optical theorem [23] [24] to relate the total reaction cross section to the angular elastic scattering cross section [25]. This method requires good angular resolution and statistics, particularly at small forward angles. Other methods rely on theoretical models such as that by Jiang, Rehm, Back, and Janssens[26]. The theoretical models can differ by up to two orders of magnitude for a kinetic energy of 1.5 MeV [8]. This is partly due to the influence of resonances at these energies, and the variations in the available cross section datasets mentioned above, especially at energies below about 3 MeV [26]. Some datasets, notably that of Mazarakis and Stephens [1] fall off less than would be expected for the Coulomb barrier. This would be consistent with the phenomenon

of "absorption under the barrier" which allows some fusion to initiate at distances greater than the nuclear radius. Other datasets such as that of Becker et al. [3] do not appear to have this feature, which seems to give evidence against absorption under the barrier. The existence or absence of absorption under the barrier should not affect the branching ratios however.

2.6 Branching Ratios

The ^{12}C $+^{12}$ C reaction can proceed through several channels. The primary two channels which are energetically possible at any ^{12}C $+^{12}$ C energy are $^{12}\mathrm{C}(^{12}\mathrm{C},\alpha)^{20}\mathrm{Ne}$ and $^{12}\mathrm{C}(^{12}\mathrm{C},\mathrm{p})^{23}\mathrm{Na}$. At higher energies the reaction $^{12}\mathrm{C}(^{12}\mathrm{C},\mathrm{n})^{23}\mathrm{Mg}$ also becomes important. Other possible reactions, such as those leaving an oxygen nucleus as a product, are not favored at low energies due to the large Coulomb barrier present in these exit channels.

The relative probability of each exit channel is referred to as the "branching ratio" of that channel. The branching ratio is defined by the ratio of the cross section of the reaction leading to a specific exit channel to the sum of all cross sections of reactions leading to any exit channel. As a result, the sum of the branching ratios of all of the exit channels is one. In the present context, the branching ratio gives the probability that a specific nuclei such as ^{20}Ne is produced given that two ^{12}C nuclei fuse into a compound nucleus.

$$\text{Branching Ratio} = \frac{\sigma_{channel}}{\sigma_{sum}} \tag{2.9}$$

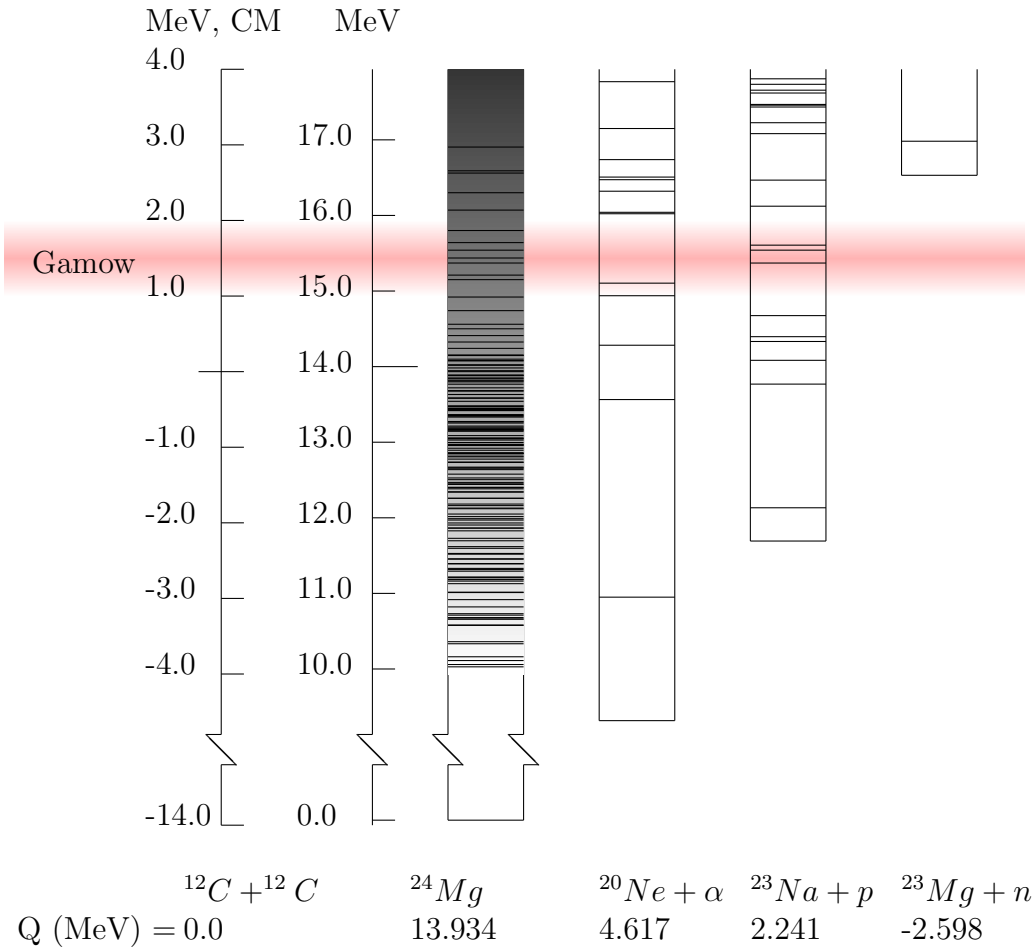

Figure 2.2: Level Diagram for the isotopes of interest. The approximate location of the Gamow window is shown by the horizontal band.

Reaction	Q Value (NNDC [10])	Coulomb Barrier (Exit Channel) (Bass [27][28])	Difference
$^{12}C + ^{12}C$		5.413 MeV	
$^{12}C(^{12}C,\gamma)^{24}Mg$	13.934 MeV	0 MeV	13.934 MeV
$^{12}C(^{12}C,\alpha)^{20}Ne$	4.617 MeV	3.005 MeV	1.612 MeV
$^{12}C(^{12}C,p)^{23}Na$	2.241 MeV	1.715 MeV	0.526 MeV
$^{12}C(^{12}C,n)^{23}Mg$	-2.598 MeV	0 MeV	-2.598 MeV
$^{12}C(^{12}C,^{8}Be)^{16}O$	-0.205 MeV	4.813 MeV	-5.018 MeV
$^{12}C(^{12}C,2\alpha)^{16}O$	-0.112 MeV	2*2.427 MeV	-4.966 MeV

Table 2.3: Carbon-Carbon Reactions. The Coulomb barrier is given with 0 MeV associated with the products at infinite separation. The difference between the Q value and the Coulomb barrier is one measure of how open a channel is. For example, $^{12}C(^{12}C,^{8}Be)^{16}O$ is energetically possible starting at 205 keV, but the Coulomb barrier makes it an unlikely reaction up to around 5 MeV. Note that all the reactions must pass through the same entrance channel listed on the first line.

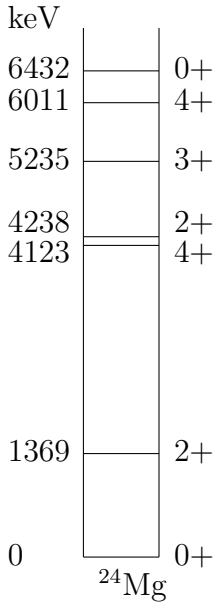

Figure 2.3: ^{24}Mg Level Diagram

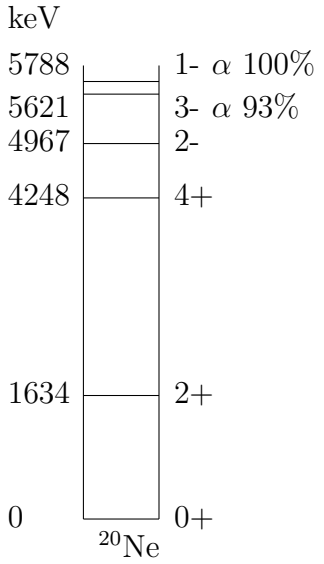

Figure 2.4: ^{20}Ne Level Diagram

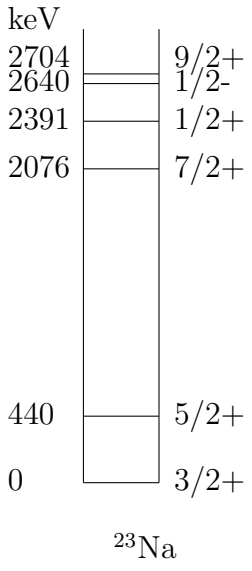

Figure 2.5: ^{23}Na Level Diagram

An idea of which exit channels are important can be developed by looking at the Coulomb barriers and Q values for each reaction. These are shown in Table 2.3 and a level diagram for the A = 24 system is shown in Figure2.2. If the Q value plus the initial kinetic energy is less than the Coulomb barrier then the emitted particle would have to tunnel through the Coulomb barrier. This would make the exit channel much less favorable and greatly diminish its branching ratio. If the Q value plus the initial kinetic energy is negative, then the exit channel is not energetically possible. Additionally, since nuclear forces are much stronger than electromagnetic forces, channels which emit particles will be favored to those which emit gamma rays when there is sufficient energy for the emitted particles to clear the Coulomb barrier. This is why ^{24}Mg is not a major exit channel for the ^{12}C +^{12} C reaction despite the high Q value and the absence of a Coulomb barrier for the gamma ray.

The Q value is the energy released during the reaction. It is calculated by comparing the mass of the reactants to the mass of the products and using $E = mc^2$ to convert the mass lost into energy released. Since the mass that is converted to energy is much less than the total mass of the nucleons involved in the reaction, the binding energy per nucleon is usually tabulated instead of the absolute masses. In this case the energy released is equal to the increase in total binding energy for reactions that do not create new particles. Using the reaction ^{12}C(^{12}C, α)^{20}Ne as an example (binding energies are from [29]),

^{12}C Binding energy per nucleon:	7680.144 keV
^{20}Ne Binding energy per nucleon:	8032.24 keV
^{4}He Binding energy per nucleon:	7073.915 keV
^{12}C +^{12} C Total binding energy:	2*12*7680.144 keV= 184324 keV
^{20}Ne +^{4} He Total binding energy:	20*8032.24 keV+4*7073.915 keV= 188941 keV
Total binding energy increase (Q value):	4617 keV

The values listed in Table 2.3 were calculated with the aid of the Q-value Calculator available on the NNDC website[10].

The Coulomb barrier for Table 2.3 is found by finding the maximum of the nuclear plus Coulomb potentials. Here r refers to the center to center separation distance of the two nuclei. The barrier is calculated for a head-on collision so there is no angular momentum term needed.

$$V(r) = V_c(r) + V_n(r) \tag{2.10}$$

The Coulomb potential is that of two positive point charges brought together, using the potential at infinite distance as the reference zero potential.

$$V_c(r) = \frac{1}{4\pi\epsilon_0}\frac{Z_1 Z_2 e^2}{r} \tag{2.11}$$

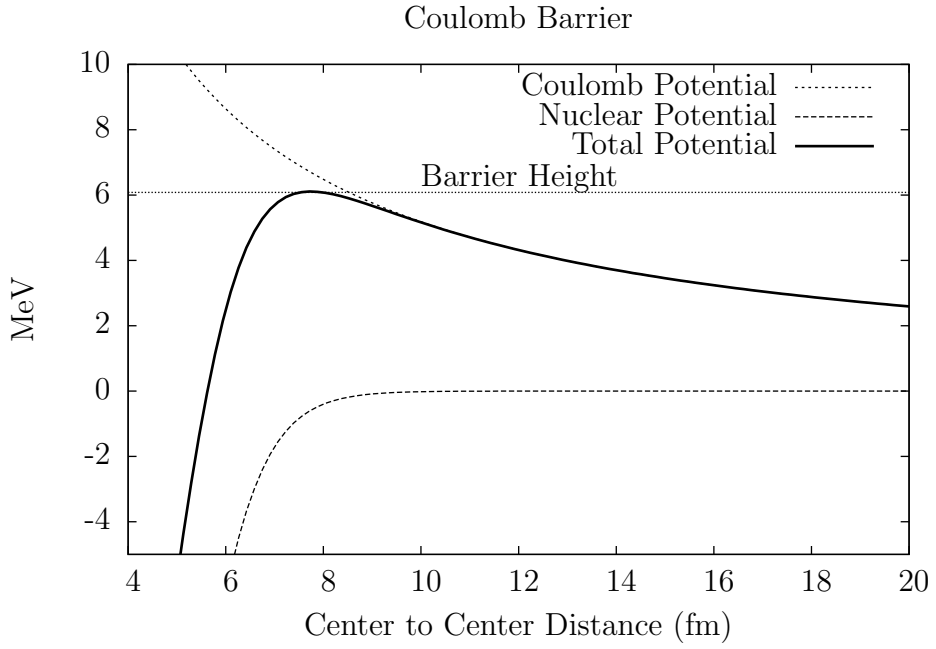

Figure 2.6: The potential energies seen by two nuclei as a function of center to center separation distance. The potential energy at infinite separation is shown as 0 MeV. This particular plot is for ^{12}C +^{12} C.

A rough approximation for the nuclear potential is that of a square well with a diameter equal to the sum of the radii of the two nuclei. This results in a sharp peak at this distance and the exact value of the peak is very dependent on the approximation of the nuclear radius. This approximation can be improved by using a more realistic nuclear potential with a rounded edge. The nuclear potential used to find the Coulomb barrier is the 1977 model by Bass [28].

$$-V_n(s) = \frac{R_1 R_2}{R_1 + R_2} \left(C e^{s/d_1} + B e^{s/d_2} \right)^{-1} \tag{2.12}$$

where

$$\begin{aligned} r &= \text{Center to Center distance} \\ C &= 0.0300 \text{ fm/MeV} \\ B &= 0.0061 \text{ fm/MeV} \\ d_1 &= 3.30 \text{ fm} \\ d_2 &= 0.65 \text{ fm} \\ s &= r - R_1 - R_2 = \text{Surface separation distance} \end{aligned}$$

and

$$\begin{aligned} R &= aA^{1/3} - b^2(aA^{1/3})^{-1} = \text{the nuclear radius} \\ a &= 1.16 \text{ fm} \\ b^2/a &= 1.39 \text{ fm} \\ A &= \text{the atomic mass of the nucleus.} \end{aligned}$$

Finally, equations 2.11 and 2.12 are inserted into equation 2.10. The peak location is found where the derivative with respect to the separation distance (or equivalently the center to center distance since this is offset by a constant) is zero, and evaluating the potential at this location gives the height of the Coulomb barrier. A graphical representation of the potential energies is shown in Figure 2.6.

Measurements of the branching ratio (in the form of total reaction rate for each branch) have been made using the direct $^{12}\text{C} + ^{12}\text{C}$ reaction at energies above 2 MeV [1] [3] [4]. These measurements, particularly above 2.5 MeV are used as a benchmark to check the results of the current experiment. These previous measurements can generally be divided into those which include the contribution of the ground state products directly and those which detect characteristic gammas, which require the product to be in an excited state in order to be counted.

Converting the gamma measured ratios into a total branching ratio for each branch requires a knowledge of the fraction of the product nuclei that are created in an excited state and decay through the first excited state to produce the 1634 keV (for $^{20}\text{Ne} + \alpha$) or 440 keV (for $^{23}\text{Na} + \text{p}$) gamma ray. At energies where direct particle measurements of individual states have been made, this ratio can be obtained. To make a measurement at lower energies however this data is not available. A surrogate measurement is one method of providing this missing piece of information.

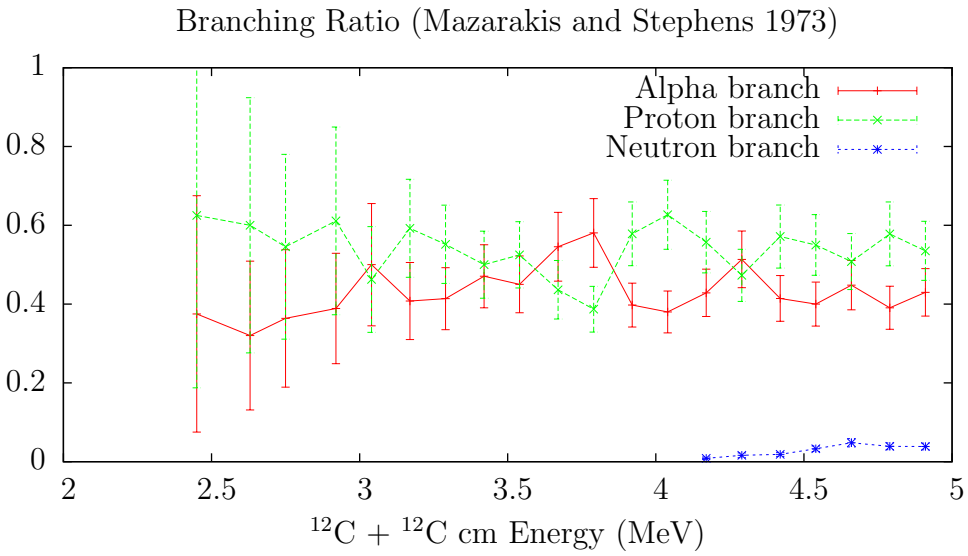

Figure 2.7: Branching ratios using the measurements of Mazarakis and Stephens[1]. These measurements detected the outgoing alpha particles and protons, which allowed the direct measurement of the ground state contribution.

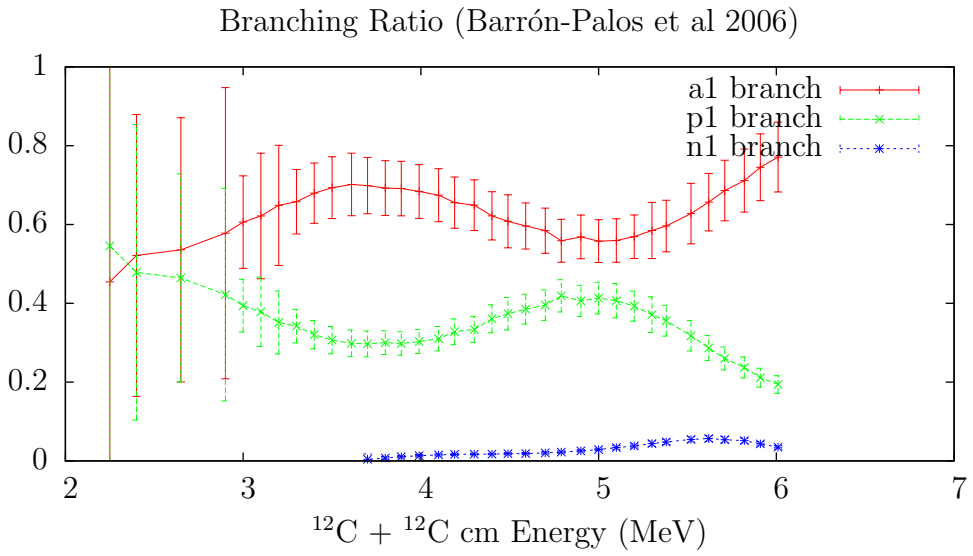

Figure 2.8: Branching ratios using the measurements of Barrón-Palos et al.[4]. These measurements used characteristic gammas and do not directly include the ground state contribution. This plot does not include the ground state contribution. Converting this data to a total branching ratio for the alpha, proton, and neutron branch requires a knowledge of what fraction of each daughter isotope is created and de-excites through the first excited state.

Chapter 3

Surrogate Method

Many cross sections are difficult to measure directly for various reasons. The surrogate method has been used to measure fission and other cross sections for a number of heavy nuclei by the STARS/LiBerACE [11], STARLiTe, and STARLiTeR groups. For a number of these experiments, direct (n, f) measurements were impractical due to the short half life of the target nuclei, requiring other reactions on neighboring nuclei ("surrogate reactions") to be measured in order to infer the desired (n, f) cross section.

The surrogate method relies on the existence of an intermediate state called the compound nucleus which is a mixture of the beam and target particles' nucleons. The energy of the particles is in thermodynamic equilibrium and individual particles are not identified by their origin in the target nucleus or the beam nucleus. This hypothesis allows the conclusion that the same compound nucleus can be produced for study using a number of beam and target pairings[11]. The key items to match in the compound nucleus are the number of protons and neutrons, the excitation energy, and spin distribution. The best entrance channel to use is a compromise between getting the closest matching compound nucleus and choosing beam and target nuclei which are experimentally feasible to work with.

In the case of ^{12}C $+^{12}$ C reactions, the compound nucleus is ^{24}Mg. The Q value going to the compound nucleus is just under 14 MeV. Since the stellar reactions of interest occur at energies around 1.5 MeV, a typical excitation energy of interest in the compound nucleus is around 15.5 MeV. A formation reaction that produces ^{24}Mg in a range of excitations between about 14 and 20 MeV is desired.

To further improve the measurement, angular momentum should be considered. Angular momentum comes into the compound nucleus in two ways. One is from the intrinsic spin of the colliding particles. The ^{12}C nucleus has an intrinsic angular momentum of 0, making this contribution 0 for ^{12}C $+^{12}$ C reactions. The other contribution comes from the orbital angular momentum of the impact. A convenient image for this contribution is two balls hitting each other either head on or receiving a glancing blow, then being glued together on impact. The head on case delivers no angular momentum, while the glancing blow would provide the maximum angular momentum. Using this model and typical estimates for the

radii of a ^{12}C nucleus leads to spins up to 3ħ to 4ħ.

The difference in the reaction rates as a result of this potential spin difference can be neglected if certain criteria are met [30]. A primary condition is that the excitation energy must be sufficiently high that the possible branches are dominated by level density integrals rather than individual states [31]. This independence of the branching ratios from spin and parity is called the Weisskopf-Ewing approximation. For carbon burning reactions this is met for the compound nucleus but not for the daughter nuclei, therefore matching the spin distribution for the compound nucleus is still important to minimize the change in branching ratios that may occur due to different spin distributions.

Several reactions can be considered. The first is the direct method using $^{12}\mathrm{C} + ^{12}\mathrm{C}$. This method requires very high beam currents at low energies due to the Coulomb barrier. Measurements using this method are discussed in Chapter 2 Section 2.5. Similarly, other reactions with two larger atoms such as $^{14}\mathrm{N} + ^{10}\mathrm{B}$ would generally see similar Coulomb barriers and not escape the fundamental difficulty with $^{12}\mathrm{C} + ^{12}\mathrm{C}$.

The reactions $^{20}\mathrm{Ne} + \alpha$ and $^{23}\mathrm{Na} + \mathrm{p}$ both bring in smaller amounts of angular momentum from the collision (though the sodium reaction has intrinsic momentum it brings in) and do not have prohibitive Coulomb barriers. However, to scan different amounts of excitation in the compound nucleus using these reactions would require many runs using different beam energies. Also, the channels to be measured would often have the same signature in the detector as scattering reactions. For example if the compound nucleus was populated with the reaction $^{20}\mathrm{Ne} + \alpha$ and the outgoing alpha channel was measured, the result is a scattering measurement. Separation of the compound component and other components to the scattering cross section (ie, elastic, direct inelastic, or pre-equilibrium inelastic) makes this approach not ideal.

The approach that was selected is to excite ^{24}Mg using inelastic scattering. Using inelastic excitation allows for the scattered particle to be used to identify the excitation produced in the surrogate compound nucleus[1]. By identifying the excitation of the compound nucleus on a per event basis the correct excitation distribution can be reconstructed for a range of different stellar temperatures.

Lighter ions are preferred for the inelastic excitation for a few reasons. First is that lighter ions will provide a much clearer signature in a deltaE-E silicon detector setup after scattering. Second, lighter ions will produce less angular momentum during collision. Due to the beam needing a much higher energy than the kinetic energy of the $^{12}\mathrm{C} + ^{12}\mathrm{C}$ reaction, a tendency towards higher angular momenta needs to be counteracted. Using Talys[32] calculations, protons will produce angular momenta greater than 4 around 15% of the time at 30 MeV while alpha particles will produce angular momenta greater than 4 around 35% to 45% of the time. Therefore on reducing the higher spin population alone protons are slightly

[1]Since inelastic excitation does not combine two nuclei, referring to the resulting excited nucleus as a compound nucleus is not standard notation. The notation is kept here to emphasize the intended parallel between the excited ^{24}Mg nucleus produced by inelastic excitation and the nucleus produced by combining two ^{12}C nuclei.

favorable, however alpha particles were ultimately selected because they would favorably populate the same parity pattern (0+, 2+, etc.) and because the scattered alpha particles have a convenient stopping range in the silicon detector setup.

Chapter 4

Experimental Setup

4.1 Overview

Three experimental runs were performed. The first took place at the LBNL 88" Cyclotron starting March 12, 2011 and ending the following day. This run was intended to be a test run which would support a longer run if the results looked favorable. The second run was at the TAMU K150 (88") Cyclotron at the Texas A&M Cyclotron Institute and ran from December 4, 2012 to December 12, 2012. Data from this run had problems with unexplained low energy particles being detected, and it was eventually decided that the measurement needed to be repeated. The third and final run was also at the TAMU K150 Cyclotron and took place from November 11, 2014 until November 18, 2014. Data from this final run at TAMU was used for the analysis.

The LBNL run made use of the STARS/LiBerACE [33] target chamber and detector system. The Texas A&M runs made use of the STARLiTeR system, which is an upgrade of the STARS/LiBerACE system previously located at LBNL. The system includes the STARS target chamber which holds the silicon detectors and target under vacuum and in line with the particle beam, up to six germanium detectors each within a BGO detector whose purpose is to veto Compton scattering events in the germanium detector, and the electronics necessary to record the signals from each detector. During operation, a master trigger is generated which causes the readout for all detectors. For this experiment, the master trigger was generated by a coincidence of the two downstream silicon detectors, described in Section 4.4.

4.2 Beam

An alpha particle beam with a nominal energy of 40 MeV was used for all three runs. During analysis, the beam energy was considered a free parameter which was fitted using the energy of scattered beam at different angles for the various target masses (^{12}C, ^{24}Mg, and ^{208}Pb). The fitted values were close to the 40 MeV nominal value. The value adopted for

the final TAMU run was 39.58 MeV at the beginning of the run and 39.33 MeV at the end of the run. The change in the fitted value occurred over a period of about 24 hours during the middle of the week long run. Fits within each stable period had a scatter of approximately 0.07 MeV. The cause of the change was not positively identified.

The beam current was adjusted to be in the range of 1 to 1.5 nA for the first run and in the range of 0.5 to 2 nA for the second two runs when the primary ^{24}Mg target was in place. Trigger rates for the silicon detectors were the limiting factor for beam current. The final run at TAMU went though several periods when the beam current would oscillate by a factor of two or more. Efforts were made by the staff to smooth these oscillations when they occurred. These oscillations had the potential to affect the energy calibration of the detectors by causing the count rate to oscillate with the beam current and exceed the desired maximum count rate, however this was not seen in the analysis and the data during these periods of current oscillation appears to be valid. The beam current for other targets (carbon, mylar, etc.) were adjusted such that the trigger rate was similar to that of the main target, which was typically around 7 to 10 kHz.

4.3 Targets

The STARS chamber[33] is designed to hold up to eight targets. A knob is located outside the target chamber which can be manually turned in order to select which target is in the beam line. Each experiment had a different but similar array of targets which were used during the experiment, including a primary ^{24}Mg target, a carbon target for beam diagnostics and carbon subtraction, and phosphors and an empty frame for tuning. Targets present for each run are listed in Table 4.3.

The LBNL test run and the second TAMU run both used a thin, self supporting ^{24}Mg target as the primary target. Several self supporting magnesium targets were made prior to the LBNL run in an attempt to bring the thickness down as much as possible. The magnesium used for the enriched targets was obtained from Oak Ridge National Laboratory and was $99.9\% \pm 0.02\%$ ^{24}Mg. Other isotopes and impurities in the original material are listed in Table 4.1 and Table 4.2. These targets were made by using evaporation deposition of magnesium onto glass slides coated and buffed with Liquinox soap which was used as a release agent, with the intent of removing the magnesium by "floating," or slowly dipping the glass slide at an angle into water, which would lift the magnesium and hold it on the surface of the water with surface tension. This floating process is commonly used for carbon foils. In practice the magnesium did not lift in this manner. The foils were instead removed by scraping a razor along the glass, creating a rolled tube of magnesium. This rolled tube was unrolled by placing it on a piece of plastic which was then given a small electrostatic charge using a cotton swab. Once the foil was unrolled, a glue-coated target frame was placed directly on top of the foil and slowly lifted. The main target was the thinnest target produced using this method. Targets at this thickness were easy to tear during the scraping process and

Isotope	Atomic Percent	Precision
^{24}Mg	99.90	0.02
^{25}Mg	0.07	
^{26}Mg	0.03	

Table 4.1: Isotopic abundances for the enriched magnesium

all thinner attempts tore. The thinnest target successfully produced was used as the main target for both the LBNL run and the second TAMU run. The target thickness was measured two ways. The first was using a second glass slide coated at the same time as the main target. This slide was measured to be 174 ug/cm^2 at the center using a profilograph. The thickness was also measured using an alpha source and a silicon detector and relating the energy lost by the alpha to the thickness of the target. This measurement gave a thickness of 155 ± 10 ug/cm^2. Since this experiment is designed to measure ratios, the primary importance of the thickness measurement is to properly account for the energy lost by the particle within the target. Using a thin target minimizes this energy loss and the associated energy uncertainty.

The main target for the first TAMU run was made by coating a thin, mounted natural carbon backing with magnesium. The motivation for this was that the total target thickness could be lower than the thinnest freestanding magnesium target. Enriched ^{12}C foils were intended as the backing, but only foils from an older production run could be obtained and these foils disintegrated during the floating process. The main target for this run was 89 ug/cm^2 on a carbon backing with a nominal thickness of 50 ug/cm^2. The magnesium thickness was measured using a glass plate coated at the same time as the carbon backing by a profilometer. During the experiment a natural carbon target from the same batch as the carbon backing was used with the intent of subtracting the effects of the carbon backing. Difficulties with the data from the first TAMU run led to the decision to return to the older freestanding target for the second run, though it is not clear what role the carbon backing played in the data.

Element	ppm	Element	ppm	Element	ppm
Be	< 10	Rb	< 200	Eu	< 50
B	< 100	Sr	< 100	Gd	< 200
Na	300	Y	< 50	Tb	< 500
Al	< 100	Zr	< 200	Dy	< 1000
Si	< 100	Nb	< 500	Ho	< 500
K	< 100	Mo	700	Er	< 50
Ca	< 100	Ag	< 50	Tm	< 500
Ti	< 100	Cd	< 500	Yb	< 20
V	< 100	In	< 500	Lu	< 50
Cr	< 100	Sn	< 100	Hf	< 500
Mn	< 100	Sb	< 500	Ta	< 500
Fe	< 100	Cs	< 500	W	< 500
Co	< 100	Ba	< 100	Pt	< 500
Ni	< 100	La	< 200	Au	< 500
Cu	< 100	Ce	< 1000	Hg	< 500
Zn	< 500	Nd	< 1000	Pb	< 200
Ga	< 200	Pr	< 1000	Bi	< 200
Ge	< 200	Sm	< 1000		

Table 4.2: Impurity elements present in the enriched magnesium

Description	Accumulated Charge	Beam Time
LBNL Run		
Natural Mg (Label 8B)		20 minutes
^{24}Mg (Label 12) (262 ug)		(not used)
^{24}Mg (Label 14) (155 ug)		2083 minutes
Mylar		39 minutes
Natural Carbon		118 minutes
Tantalum Frame		7 minutes
Phosphor		(Tuning)
Phosphor with 0.25 inch hole		(Tuning)
TAMU Run 1		
^{24}Mg (89 ug nominal) on $^{\text{nat}}$C (50 ug nominal)		147 hours
Natural Carbon (35 ug nominal)		14 hours
Tantalum Frame		17 minutes
Phosphor		(Tuning)
Phosphor with 0.25 inch hole		(Tuning)
TAMU Run 2		
^{24}Mg (Label 14) (155 ug)	620 μC	109 hours
^{24}Mg (Label 12) (262 ug)	11.1 μC	138 minutes
Natural Carbon (50 ug)	29 μC	315 minutes
Mylar (2 mil)	132 nC	86 minutes
^{208}Pb	630 nC	64 minutes
Tantalum Frame		(Tuning)
Phosphor		(Tuning)
Phosphor with 0.25 inch hole		(Tuning)

Table 4.3: Targets used for each run and the approximate amount of beam each target received. The analyzed data is from TAMU Run 2.

4.4 Silicon Detectors

Micron Semiconductor "S2" type silicon detectors were used to detect and measure the outgoing charged particles. These detectors are disk shaped, with a hole in the center for the non-scattered beam to pass through. The silicon is divided into 48 rings and 16 sectors which allows for the (polar) angle from the beam and (azimuth) angle around the beam to be recorded. This segmentation also allows for a single detector to record multiple particle hits. The inner ring is located at a radius of 11 mm and the outer ring at 35 mm, making each ring 0.5 mm wide. The STARS chamber allows up to four of these detectors to be mounted and gives flexibility to the mounting position of each. A typical mounting arrangement is a "dE-E" arrangement. For this setup a thin (generally less than 150 μm) detector is placed in front of a thicker (generally 1 mm) detector. A scattered particle passes through the thinner "dE" detector, losing some of its energy, then deposits the rest in the thicker "E" detector. Since different particles lose energy at different rates for the same initial energy this setup can be used to identify different charged particles assuming that they have enough energy to pass through the dE, and generally assuming they do not have enough energy to pass through the E detector. The specific silicon setup for each run is shown in Table 4.4. Due to limitations on the total number of channels, signals from adjacent rings and from adjacent sectors are often paired together resulting in a detector with 24 rings and 8 sectors. This was done with all the detectors except for the dE detector in the second TAMU run.

Label	Serial Number	Thickness	Distance from Target
LBNL Run			
dE	2431-13	150 μm	20.7 mm
E1		1 mm	24.3 mm
E2		1 mm	34.8 mm
TAMU Run 1			
dE1	2587-4	62 μm	20 mm
E1	2540-24	1 mm	24 mm
dE2	2521-4	62 μm	20 mm upstream
E2	2093-1	1 mm	24 mm upstream
TAMU Run 2			
dE	2521-4	62 μm	18.75 mm
E1	2045-3	1 mm	29.00 mm

Table 4.4: Silicon Detector Arrangements. The detector distances were fit using scattering data and compared to physical measurements using calipers. Adopted values are shown. Detectors were located downstream from the target except where noted.

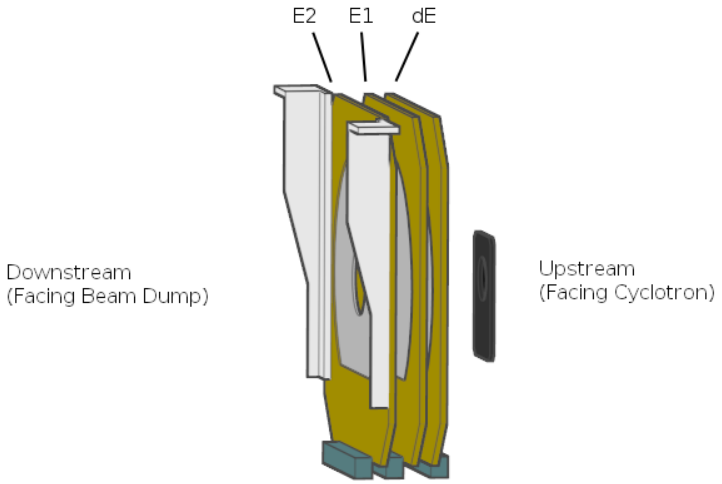

Figure 4.1: Silicon Detector Arrangement for the LBNL Run

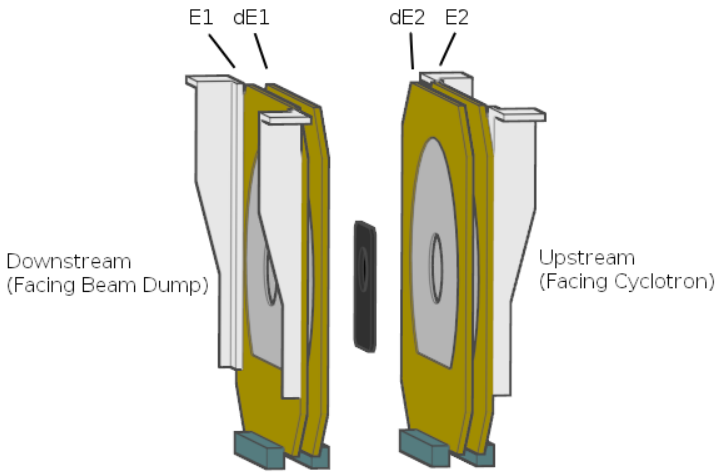

Figure 4.2: Silicon Detector Arrangement for TAMU Run 1

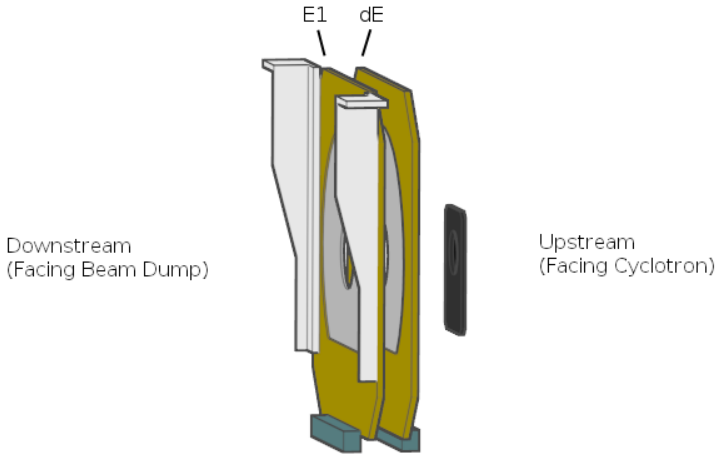

Figure 4.3: Silicon Detector Arrangement for TAMU Run 2

4.5 Germanium Detectors

Up to six segmented Canberra "clover" germanium detectors were placed around the target chamber for the detection of gamma rays emitted from the reaction. This is a typical setup for the STARLiTeR array [33]. Each clover detector consists of 4 separate cylindrical germanium crystals placed in a square with the ends facing the source. Signals from the four crystals can be summed such that the four crystals act as a single detector. Each clover detector is positioned inside a BGO detector which is used to veto clover signals resulting from Compton scattering of gammas. This veto reduces the Compton continuum present in the Clover detector while maintaining most of the full energy events. Segmented clover detectors have four germanium crystals, called leaves, arranged in a pattern resembling a four leaf clover when viewed from the end facing the target. Each leaf is separately calibrated and recorded. The leaves are also segmented into left and right halves. This allows the gamma interaction to be assigned one of four horizontal locations and one of two vertical locations. For this series of measurements the recorded energy from each crystal was summed such that each clover was treated as a single detector.

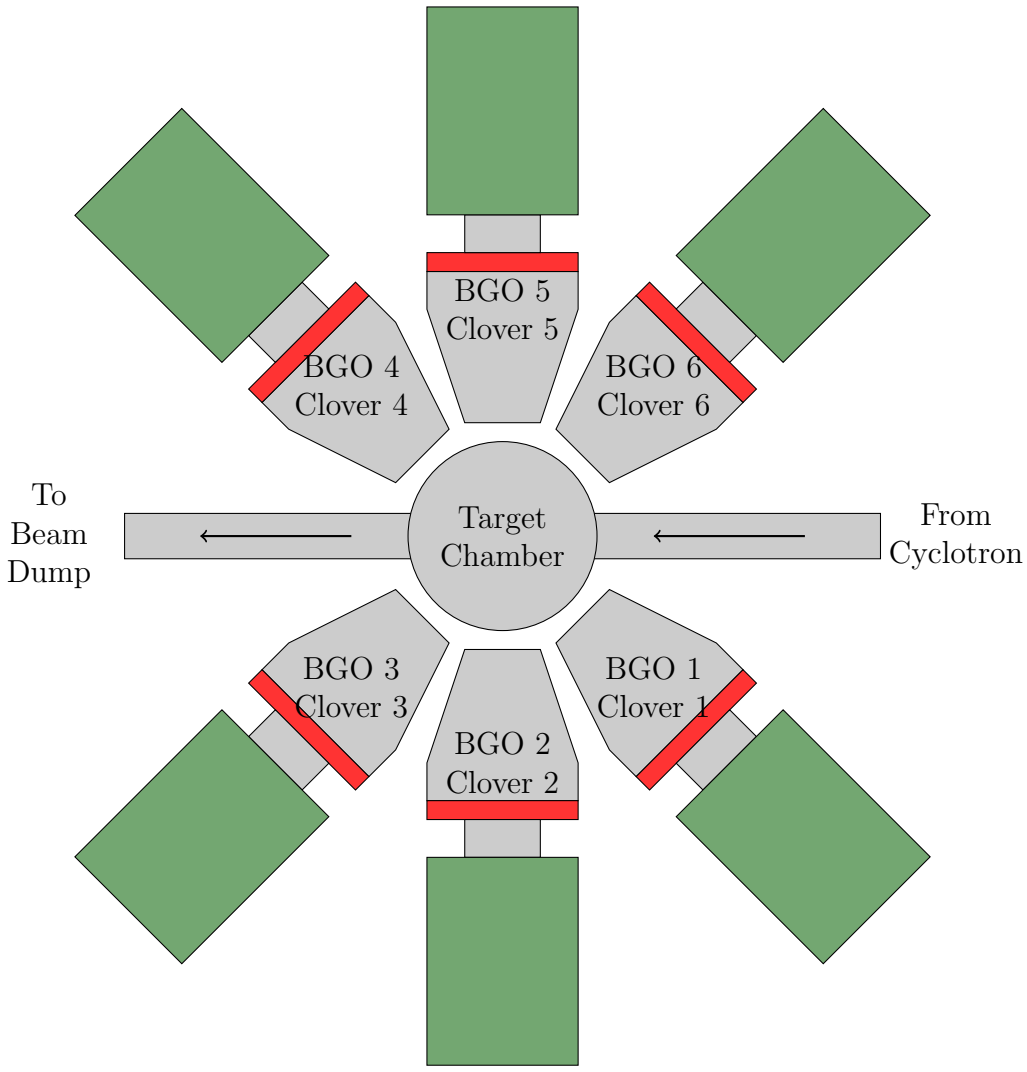

Figure 4.4: Clover detector positions as viewed from above.

Since the gamma rays of interest are emitted from nuclei that may have a recoil energy of several MeV it is necessary to apply a Doppler correction to the detected gamma energy to determine the gamma ray energy in the rest frame of the nucleus. For this purpose the two upstream and two downstream detectors were considered to be at a 45 degree angle to the beam and the final two detectors were at 90 degrees. These angles were within 5 degrees of the actual angle to the center of each detector from the target. This allowed for a sufficient Doppler correction to produce clean peaks in the gamma ray spectrum. The clover detector arrangement is shown in Figure 4.4. The velocity used for the nucleus was that found for the recoiling ^{24}Mg nucleus. The ^{20}Ne and ^{23}Na nuclei receive an additional kick from the ejected particle, but this generally a small change in velocity compared to the ^{24}Mg recoil velocity.

Most lines were well separated when they had sufficient counts to be visible. An important exception is the 1634 keV line from the first excited state of ^{20}Ne and the 1636 keV line from the second excited state of ^{23}Na. It is unlikely that these lines could be resolved even without the additional complication of the Doppler shift.

Chapter 5

Results and Analysis

5.1 ^{24}Mg Excitation Spectrum for Detected Events

The excitation of the ^{24}Mg nucleus was determined from the scattered alpha particle energy and angle. The equations used are given in Section 5.4 as Equations 5.2 through 5.8. The distribution of excited states detected is shown in Figure 5.1. Scattering events which did not lead to the detection of an alpha in the silicon detectors are not included.

Carbon was present on the magnesium target. To subtract the contribution of the carbon a natural carbon target was used in place of the magnesium target periodically throughout the experiment. The lower mass of carbon means that the recoiling nucleus takes away more energy, leaving less for the scattered alpha particle. This means that when the recoil is calculated as if it was magnesium, the ground state (elastic scattering) appears not at 0 MeV, but as a broader peak near 2 MeV, and similarly for the excited states. A scale factor was used to fit the carbon component for the magnesium target. This factor was determined by matching the number of counts in the valley between the 1369 keV state and the 4123 keV state of ^{24}Mg, an energy region where the ^{24}Mg spectrum should have no counts.

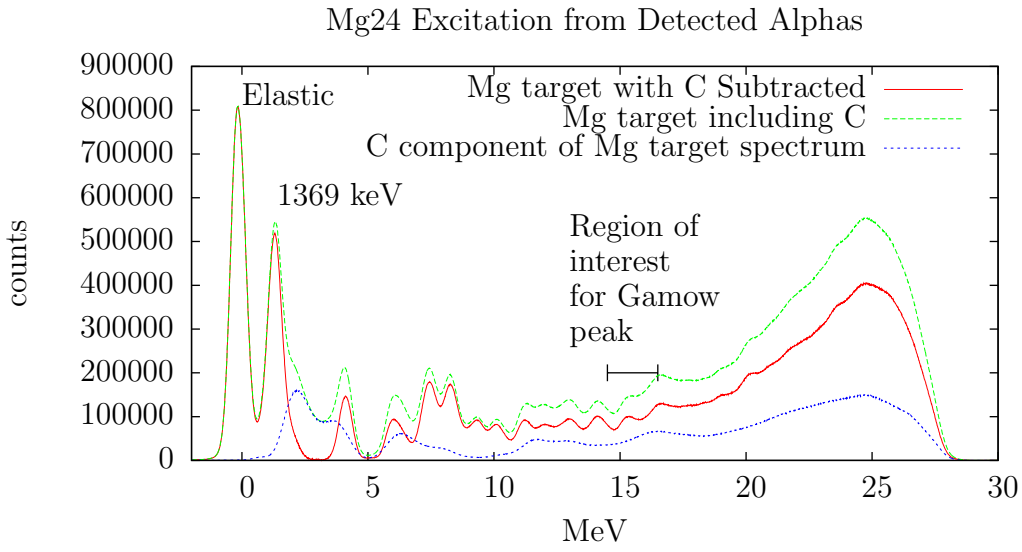

Figure 5.1: The spectrum of excitation in ^{24}Mg corresponding to detected alpha particles. This plot shows the contribution from ^{12}C before and after having been subtracted.

5.2 Gamma Ray Spectrum

For many of the excited states in the product nuclei, requiring a coincidence with a characteristic gamma allows a much cleaner identification of the outgoing channel. For the second and third excited states of ^{20}Ne, the second, third, and fifth excited states of ^{23}Na, and the first excited state of ^{23}Mg the identification was made using a coincidence between the scattered alpha and a characteristic gamma ray. The 2076 keV (second excited) state of ^{23}Na is fed by the fifth excited state requiring the fifth excited state to be determined prior to the second state and its contribution subtracted from the strength of the second state's characteristic gamma ray.

The ground state and first excited (440 keV) state of ^{23}Na could not be well separated from each other using particle data alone, though the pair was well separated from higher excited states. The 440 keV gamma ray coincident with the first excited state was used to separate the contributions of these two states.

Figure 5.2 shows the gamma ray spectrum in coincidence with any scattered alpha. Figure 5.3 shows the gamma ray spectrum in coincidence with the ^{24}Mg excitation calculated from the coincident scattered alpha. Plotting the gamma rays coincident with the ^{24}Mg excitation shows the gamma cascades present in ^{24}Mg and the onset of the particle decay channels.

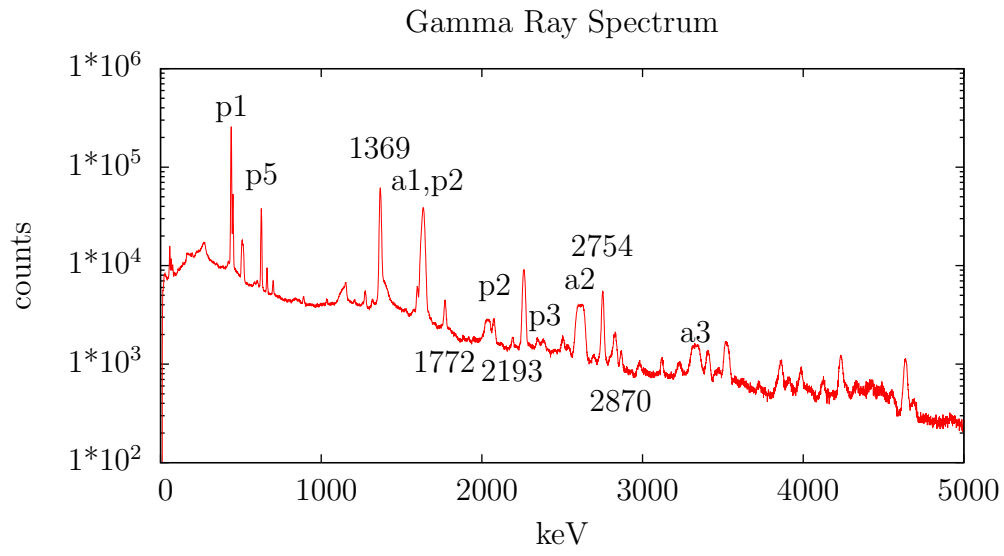

Figure 5.2: The gamma spectrum produced in coincidence with any scattered alpha. Gamma energies that correspond to states in ^{20}Ne are labeled a1, a2, and a3 for the first, second, and third excited states. Gamma energies that correspond to states in ^{23}Na are similarly labeled p1- p5. Gamma energies corresponding to states in ^{24}Mg are labeled with their energy in keV. The 1369 keV gamma corresponds to the 1369 keV state in ^{24}Mg, 2754 keV to the 4123 keV state, 2870 keV to the 4238 keV state, 1772 keV to the 6011 keV state, and 2193 keV to the 6432 keV state of ^{24}Mg.

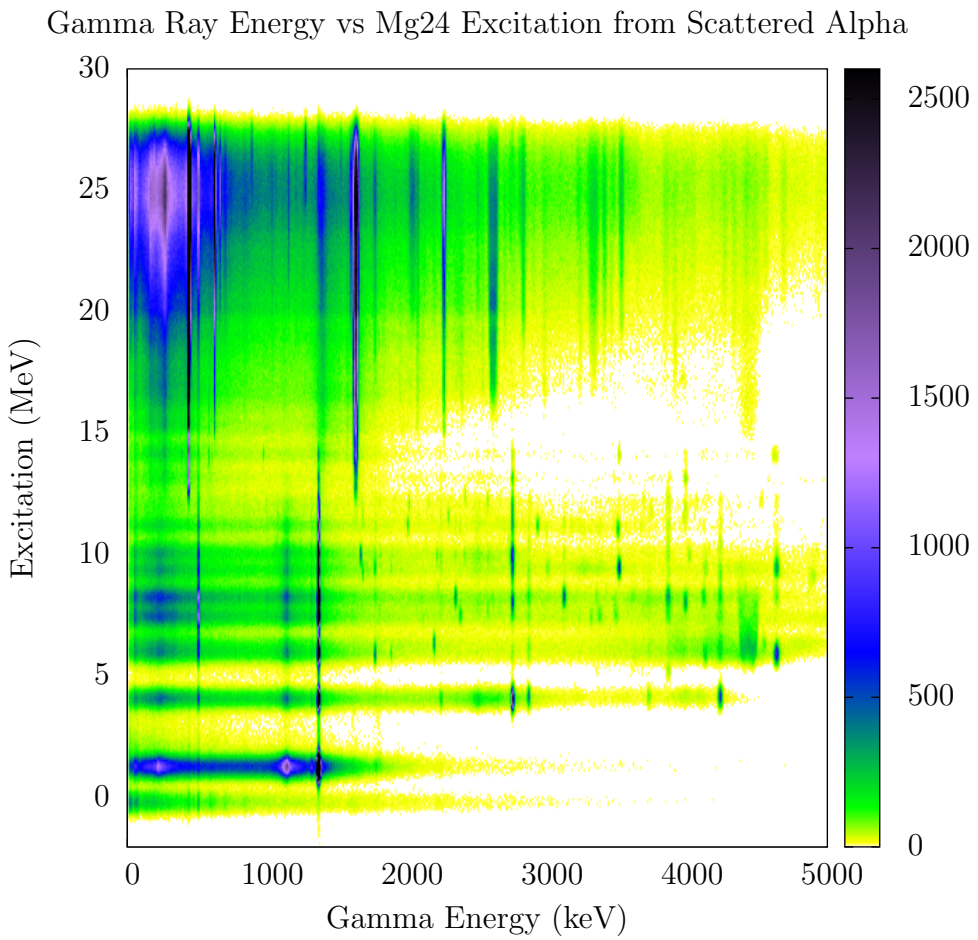

Figure 5.3: The gamma ray energies vs the excitation of ^{24}Mg as calculated from the coincident scattered alpha. The 1369 keV gamma from the first excited state of ^{24}Mg can bee seen strongly at lower excitation energies as it is fed by many of the higher excited states. At around 13 to 14 MeV excitation it can be seen to diminish in favor of the 440 keV gamma from ^{23}Na and the 1634 keV gamma from ^{20}Ne, showing the opening of the particle decay channels at higher excitation energies.

5.3 Angular Distributions

The angular distribution of the scattered alpha particles were measured for elastic and several inelastic scattering channels over the angular range covered by the silicon detectors. The total beam charge was measured at the beam dump, which was electrically insulated and acted as a Faraday cup. These measurements were compared to measurements found in the literature for the elastic and 6432 keV excited states. Since the focus of the project is to measure branching ratios and not absolute cross sections, less care was taken with the measurement of the total beam charge and exact number of target atoms. Measurements of these values were taken however and should produce scattering cross sections in rough agreement with existing measurements.

The gates for each excited state were set around the calculated excitation of the ^{24}Mg nucleus from the scattered alpha. For excited states a second condition was placed requiring the detection of a characteristic gamma ray. The gates for each state are listed in Table 5.1.

^{24}Mg State	Minimum Excitation	Maximum Excitation	Characteristic Gamma	Minimum Gamma Energy	Maximum Gamma Energy
Ground (Elastic)	-	0.7 MeV	-	-	-
1368 keV	0.6 MeV	2.0 MeV	1368 keV	1350 keV	1390 keV
4123 keV	3.4 MeV	4.8 MeV	2754 keV	2735 keV	2770 keV
4238 keV	3.4 MeV	4.8 MeV	2870 keV	2850 keV	2885 keV
6011 keV	5.3 MeV	6.8 MeV	1772 keV	1760 keV	1780 keV
6432 keV	5.8 MeV	6.8 MeV	2193 keV	2180 keV	2205 keV

Table 5.1: The ^{24}Mg excitation energy requirement and gamma ray energy requirement for the identification of the ^{24}Mg states.

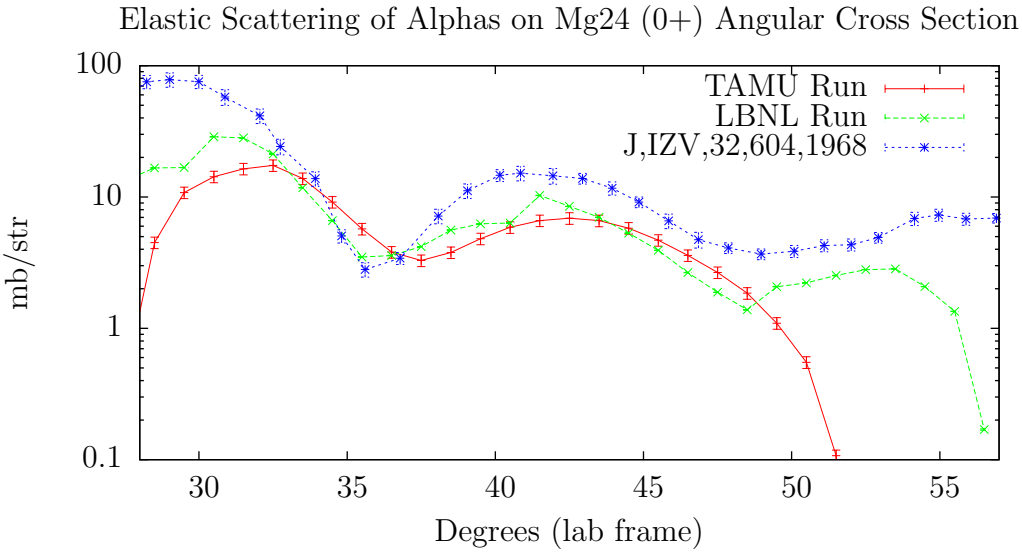

Figure 5.4: Elastic angular cross section. An existing data set taken at 40 MeV is shown for comparison. Data points below 33 degrees for both the LBNL and TAMU runs as well as data points above 47 degrees for the TAMU run and 53 degrees for the LBNL run fall off due to the edge of the detector and should not be considered valid. The error bars for the TAMU and LBNL runs denote statistical uncertainty only.

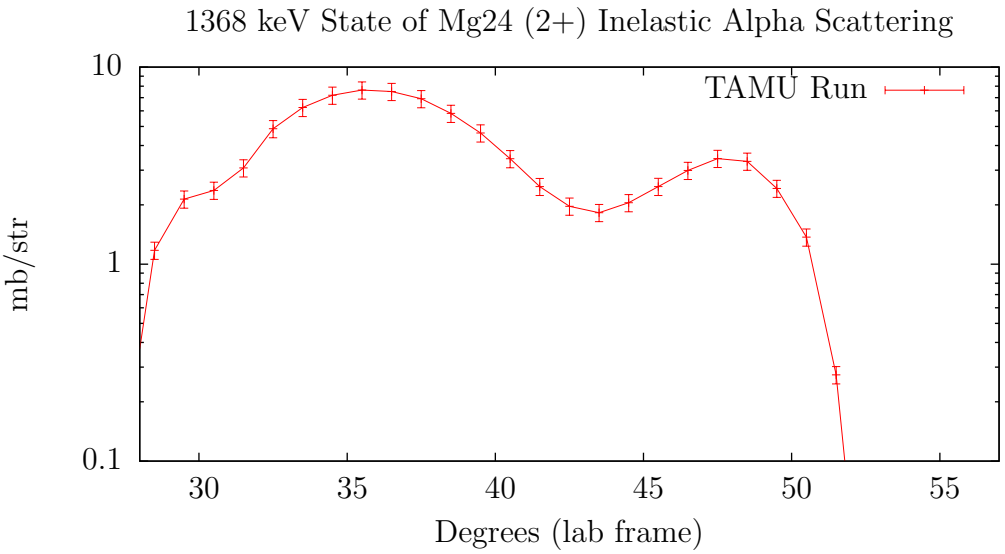

Figure 5.5: Inelastic scattering cross section for the 1368 keV excited state of ^{24}Mg. Data is shown in the lab frame of reference. The error bars denote statistical uncertainty only.

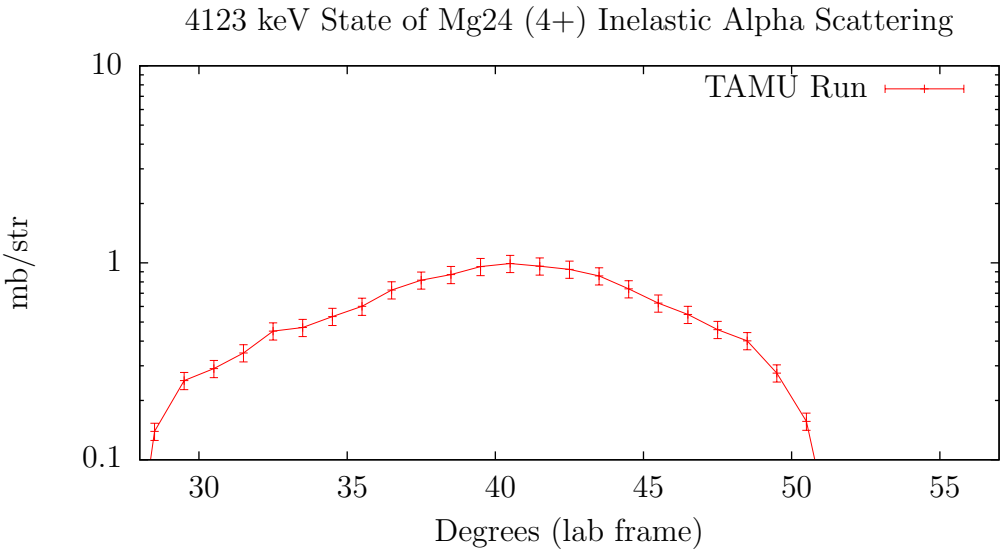

Figure 5.6: Inelastic scattering cross section for the 4123 keV excited state of ^{24}Mg. Data is shown in the lab frame of reference. The error bars denote statistical uncertainty only.

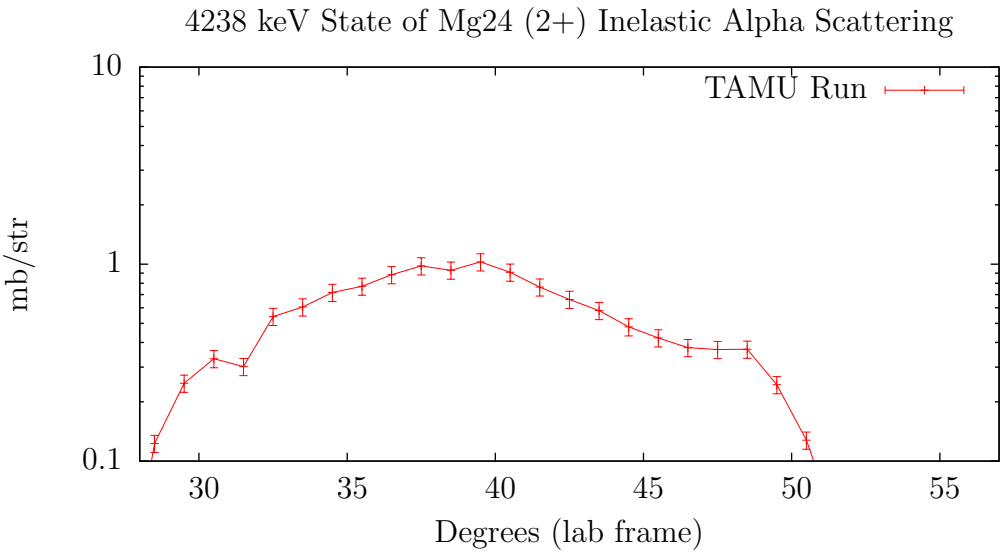

Figure 5.7: Inelastic scattering cross section for the 4238 keV excited state of ^{24}Mg. Data is shown in the lab frame of reference. The error bars denote statistical uncertainty only.

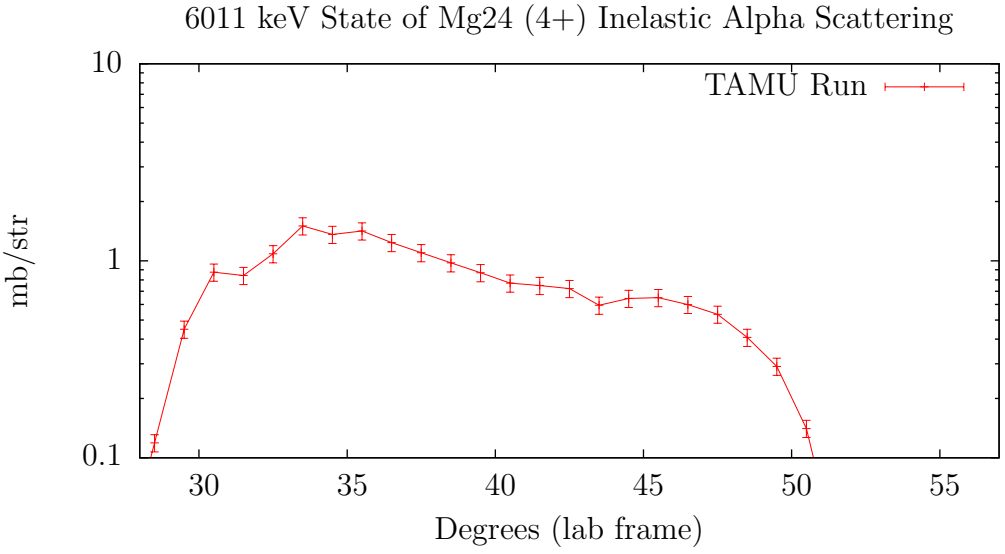

Figure 5.8: Inelastic scattering cross section for the 6011 keV excited state of ^{24}Mg. Data is shown in the lab frame of reference. The error bars denote statistical uncertainty only.

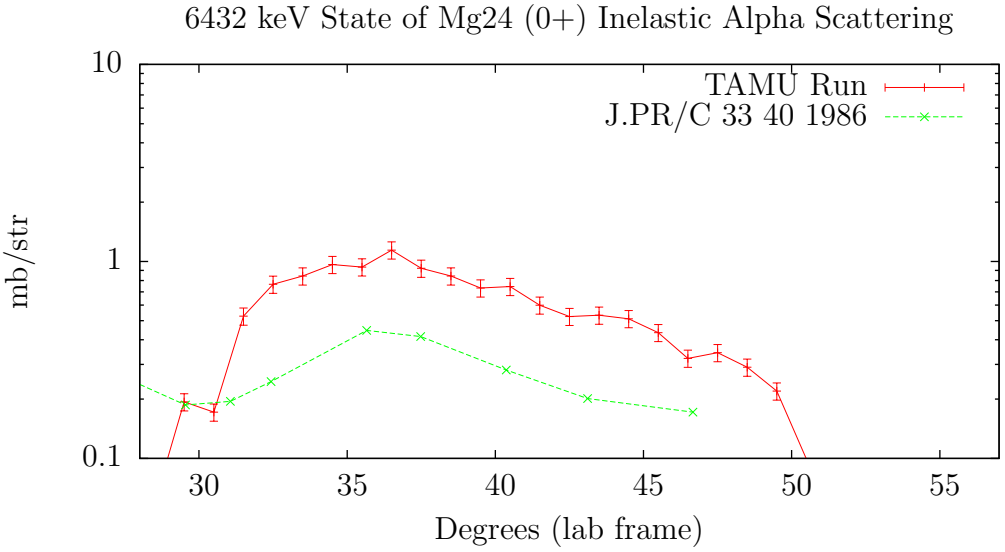

Figure 5.9: Inelastic scattering cross section for the 6432 keV excited state of ^{24}Mg. The previous data shown is from [34]. Both current and previous data are given in the lab frame of reference. The error bars for the current measurement denote statistical uncertainty only.

Inelastic scattering can proceed through either a compound reaction or a direct reaction process [35]. The compound reaction process is more likely to initially produce an excited nucleus with similar characteristics as the compound nucleus produced during carbon burning. Compound nucleus scattering will be nearly isotropic while scattering from a direct reaction will have a peaked angular distribution [35]. Figure 5.10 shows the angular distribution of scattered alpha particles which correspond to ^{24}Mg excitation energies within 1 MeV wide windows. The falloff at the low and the high ends of the angular range is due to the inner and outer edge of the detector. An offset of the beam center causes this falloff not to be a sharp line, since the lowest and highest angles will only be reached by a few sectors. The region in between is fairly flat, with a slight rise for smaller angles. Away from the detector edges the solid angle covered is proportional to the sine of the polar angle. This means that for a fully isotropic scattering distribution the total counts at 0.8 radians should be 1.27 times the total number of counts at 0.6 radians. The scattering angular distribution is thus not fully isotropic. While inelastic scattering may still have a strong compound nucleus component, this suggests that it is not fully described by compound nucleus scattering.

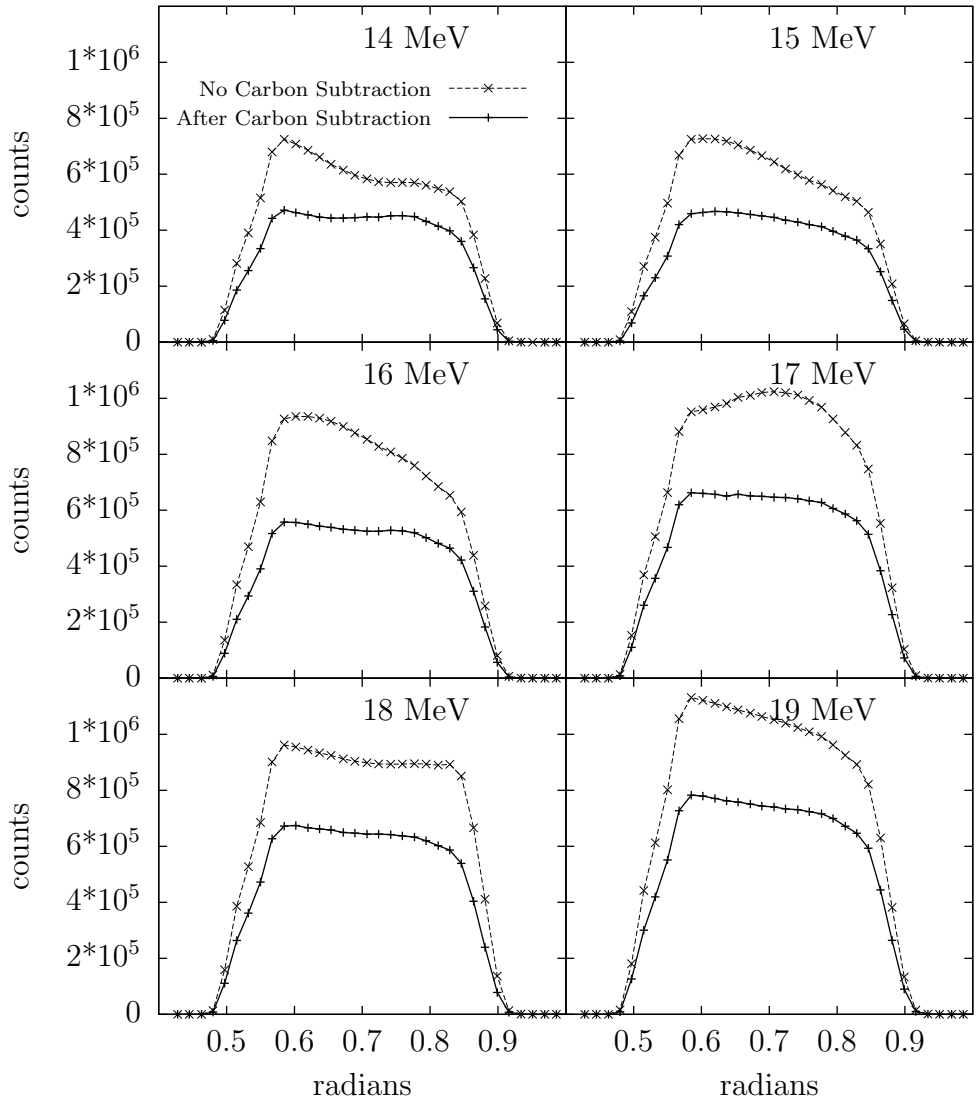

Figure 5.10: The angular distribution of alpha particles corresponding to ^{24}Mg excitation energies in 1 MeV wide bins centered on the energy given.

5.4 Channel Identification and Branching Ratios

Identifying the excitation produced in the ^{24}Mg nucleus, the daughter nucleus produced, and the excitation of the daughter nucleus relies on the scattered alpha particle from the beam and the emitted particles and gammas from the excited ^{24}Mg. The scattered and ejected alpha particles and protons are detected using the silicon detectors located inside the target chamber.

The electrical contacts on each silicon detector are divided into 48 rings on one side and 16 sectors on the other, with each ring and sector connected to its own preamp and ADC. The 16 sectors combined make a complete circle around the beam. The inner ring is located at a radius of 11 mm and each ring is 0.5 mm wide, with the last ring at a radius of 35 mm. Ideally a particle will produce a signal across one ring and one sector, though in practice small signals are often generated on neighboring rings either due to cross talk or occasionally due to a particle entering near the boundary between two rings. For the LBNL run and the first TAMU run adjacent rings and adjacent sectors were connected prior to the preamps to produce a detector with 24 ring pairs and 8 sector pairs. This was also done for the thicker E detector in the second TAMU run. This was done to reduce the number of ADC channels needed to read out the detectors. Timing (TAC) channels were also connected to rings and sectors individually, though due to a limit on the total number of TAC channels only selected rings and sectors were connected to a TAC. All rings and sectors of the dE silicon detector were connected to a TAC, while the E detector had all sectors connected to a TAC. The TAC was used to tighten the required coincidence timing window to reduce the total number of random coincidences.

The energy readings for each ring and sector were calibrated individually using a ^{226}Ra source. Silicon detectors have a near 100% efficiency for charged particles at the energies of interest that hit active areas of the detector. The efficiency of each detector is then approximately the solid angle covered by the active area of the detector. A Monte Carlo code was used to model the final efficiency for detecting each particle. This approach was used so that the forward scattering of the particles would be accounted for as well as situations such as a particle passing through the thinner dE detector but missing the thicker E detector behind it, as might happen for particles hitting the outer rings of the dE detector.

All detectors were read out when a "master gate" was produced. A master gate was produced when the downstream dE detector (labeled dE1 for the first TAMU run, dE for the LBNL and second TAMU runs) and the downstream E detector (labeled E1 for the LBNL run and the first TAMU run, E for the second TAMU run) each had at least one ring or sector signal above a threshold corresponding to approximately 500 keV.

Signals from the rings and sectors were compared while sorting the data to determine which pixels (overlaps of ring and sector) were hit. The pairing was done by comparing the calibrated energy of each ring to each sector. The ring with the energy closest to the sector was considered to be the matching ring for that hit. Rings with an energy more than 700 keV different from the sector were not considered. If adjacent rings fired their sum

Decay Reaction	Main Alpha Energy	Branch	Half Life
^{226}Ra(α)^{222}Rn	4784.34 keV	100%	1600 years
^{222}Rn(α)^{218}Po	5489.48 keV	100%	3.8235 days
^{218}Po(α)^{214}Pb	6002.35 keV	99.980%	3.098 minutes
^{214}Pb(β^-)^{214}Bi		100%	26.8 minutes
^{214}Bi(β^1)^{214}Po		99.98%	19.9 minutes
^{214}Po(α)^{210}Pb	7686.82 keV	100%	163.4 microseconds
^{210}Pb(β^-)^{210}Bi		100%	22.20 years
^{210}Bi(β^-)^{210}Po		100%	2.012 days
^{210}Po(α)^{206}Pb	5304.33 keV	100%	138.376 days
^{206}Pb			Stable

Table 5.2: The decay chain for ^{226}Ra. The first four alpha peaks in the decay chain were in secular equilibrium since the half lives of ^{222}Rn through ^{214}Po are all much less than the age of the source. The source was not old enough for ^{210}Pb to be in secular equilibrium yet and as a result the 5.3 MeV Peak from ^{210}Po was small and not used for calibrations. Data is from the NNDC website[29].

was compared to the sector in a similar way, with the higher energy ring being assigned as the corresponding ring to the hit sector. Once the corresponding ring was found for a sector, the adjacent rings were removed from the search for other sectors that might have fired. This process started with the highest energy sector and proceeded to lower energy sectors in order. Multiple hits within a single event were common, and necessary for the particle-particle coincidence measurements.

Pixels for the dE and E detectors were paired based on a ray trace window. First, the sector for the dE hit had to overlap the sector for the E hit. Second, each E detector ring pair was assigned 5 acceptable dE rings, the center of which was in line with the center of the target. If both criteria were satisfied, these signals were considered to have been produced by a single particle passing through the dE and hitting the E detector behind it. Signals that corresponded to a dE hit that was not paired to a E1 hit were kept since these hits may be particles with a low enough energy that they did not pass through the dE detector. E detector hits that did not have a corresponding dE detector hit were discarded.

Once a dE and an E hit were paired, their energies were used to determine what type of particle they were. Different charged particles lose energy at different rates while passing though the dE detector and this can be used to identify protons and alpha particles. Some deuterons and tritons were also identified this way and this identification was used to discard those events. Figure 5.11 shows the measured energy loss in the dE detector divided by the path length of the particle in the dE detector for particles of different total energy. Dividing by the path length accounts for the greater amount of energy a particle at a high angle would

EdELin Range	Assigned particle (PID)
> 3.7	alpha
$2.8 - 3.7$	^{3}He
$1.54 - 1.68$	triton
$1.27 - 1.54$	deuteron
$0.8 - 1.27$	proton

Table 5.3: Particle identification based on the EdELin parameter defined by Equation 5.1.

leave in the dE detector due to longer path through the detector.

Since the energy left in the dE detector is not a linear function of the total energy for a given particle, an empirical fit was used to convert the dE energy to a parameter that was fairly constant with energy and only varied considerably with the different energy loss rates associated with different particles. This relation is based off one used by the STARLiTeR group. The exact parameters were adjusted to fit the data. This parameterization avoids the difficulty of using curved gates on Figure 5.11. The result of this parameterization is shown in Figure 5.12 and a projection of that plot is shown in Figure 5.13.

$$\text{EdELin} = 0.001 * \left(E_{sum}^{1.8} - \left(E_{sum} - \frac{dE}{dx} * 0.15 \right)^{1.8} \right)^{\frac{1}{1.8}} \tag{5.1}$$

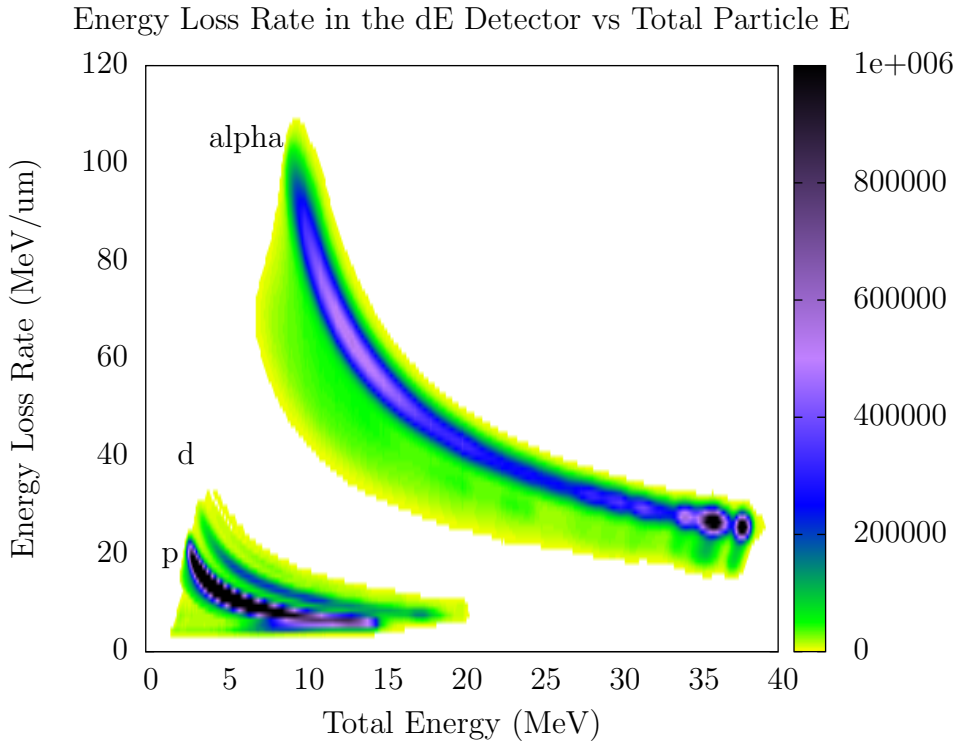

Figure 5.11: dE Energy Loss Rate vs Particle Energy for PID. Here the energy deposited in the dE silicon detector is divided by the path length of the particle through the detector. Since the dE is a thin detector, this places a particular particle on the same curve for all measured angles. The labels p and d refer to protons and deuterons. A faint band from tritons is present just above the band for deuterons. The hook in the proton band at 15 MeV is from higher energy protons passing through both the dE and E detectors, thus not depositing their full energy.

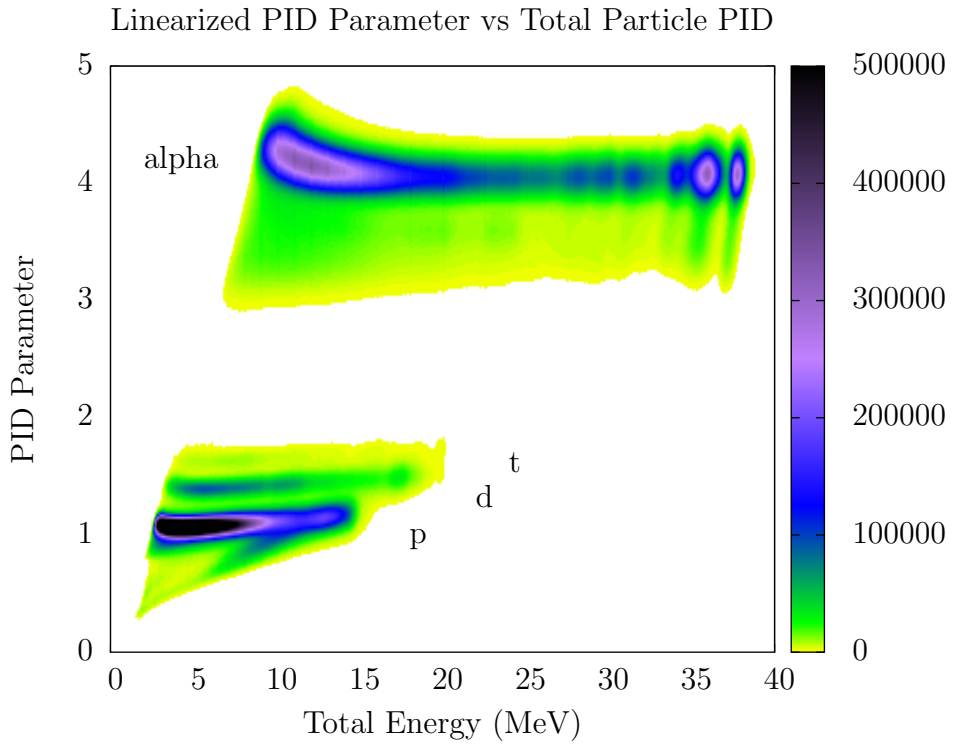

Figure 5.12: The result of applying the parameterization of Equation 5.1 to Figure 5.11. Notice that the curved bands from Figure 5.11 are now relatively flat, allowing for the particle identification (PID) bands to be defined by a minimum and maximum of one parameter rather than by limits in dEdx as a function of energy. The labels p, d, and t refer to protons, deuterons, and tritons respectively.

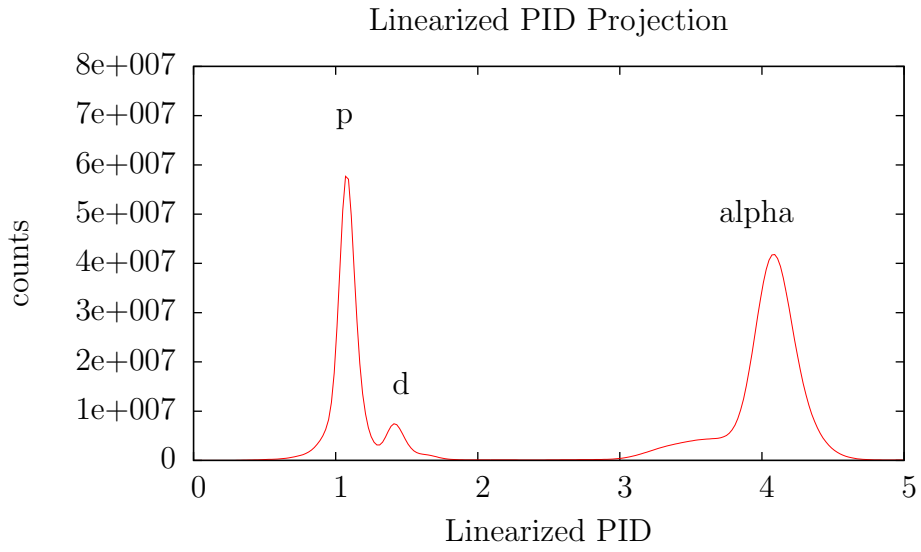

Figure 5.13: A 1D projection of Figure 5.12. The proton, deuteron, and alpha peaks are labeled.

The highest energy alpha particle was considered to be the scattered alpha particle and was used to determine the excitation of the ^{24}Mg nucleus. Events that did not have at least one identified alpha particle were discarded. The process for finding the excitation of the recoiling ^{24}Mg nucleus is shown in Equations 5.2 through 5.8. The alpha particle mass m_α and the beam energy E_{beam} are known beforehand. The beam momentum p_{beam} is known from the beam energy and the alpha particle mass. Assuming the recoiling nucleus is ^{24}Mg gives the recoil mass m_r. The scattered alpha particle energy E_s and the scattered alpha particle angle θ_s are measured using the silicon detectors. The recoil momentum m_r is found using conservation of momentum by subtracting each component of the scattered alpha particle's momentum from the momentum of the beam alpha particle prior to scattering. The energy of the recoil E_r is then known from the momentum and mass of the recoil. Finally, the difference in energy between the beam particles and the sum of the energy of the scattered alpha particle and recoiling nucleus gives the excitation of the recoiling nucleus by conservation of energy.

$$p_s = \sqrt{2 * m_\alpha * E_s} \tag{5.2}$$
$$p_{s,z} = p_s \cos(\theta_s) \tag{5.3}$$
$$p_{s,r} = p_s \sin(\theta_s) \tag{5.4}$$
$$p_{r,z} = p_{\text{beam}} - p_{s,z} \tag{5.5}$$
$$p_{r,r} = p_{s,r} \tag{5.6}$$
$$E_r = \frac{p_{r,z}^2 + p_{r,r}^2}{2.m_r} \tag{5.7}$$
$$E^* = E_{\text{beam}} - E_s - E_r \tag{5.8}$$

Where:

E_s = Scattered alpha kinetic energy
E_r = Recoiling ^{24}Mg kinetic energy
E_{beam} = Beam particle kinetic energy
E^* = ^{24}Mg excitation energy
m_α = Alpha particle mass (4.*931.5 MeV/c^2)
m_r = ^{24}Mg mass (24.*931.5 MeV/c^2)
θ_s = Angle of the scattered particle trajectory from the beam direction
p_s = Scattered alpha momentum
p_{beam} = Beam alpha momentum prior to scattering
$p_{s,z}$ = Scattered alpha momentum along the beam line
$p_{s,r}$ = Scattered alpha momentum perpendicular to the beam line
$p_{r,z}$ = Recoiling ^{24}Mg momentum along the beam line
$p_{r,r}$ = Recoiling ^{24}Mg momentum perpendicular to the beam line

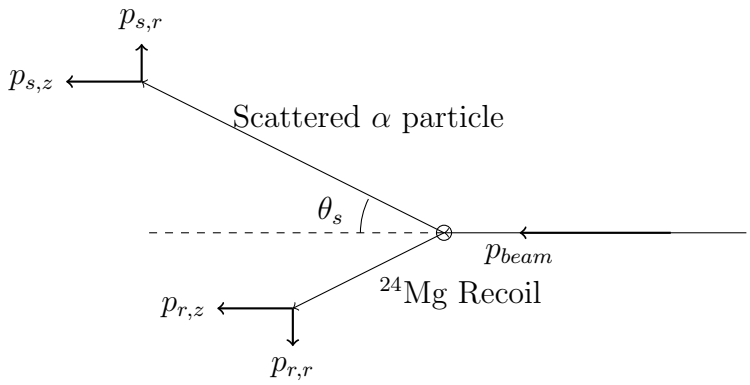

Figure 5.14: Diagram showing the scattering angle and momenta components for Equations 5.2 through 5.8.

One method of identifying the outgoing branch uses a coincidence of the scattered alpha and the ejected alpha or proton. This method is most easily understood by comparing the calculated ^{24}Mg excitation from the scattered alpha with the energy of the second particle emitted from the excited ^{24}Mg. Since these particles are typically of lower energy, many cannot be identified using the dE-E method and the identification relies on energy and angle. For the excitation versus second particle energy, shown in Figure 5.15, the angle of the second particle is not included. To include the angle information an assumption must be made about the second particle's mass. This is done in Figure 5.17 by assuming the second particle is an alpha and in Figure 5.18 by assuming the second particle is a proton.

Using these assumptions the corresponding excitation of the product ^{23}Na or ^{20}Ne can be determined using Equations 5.9 through 5.21. The energy of the ejected alpha particle or proton E_{ej}, the polar angle relative to the beam θ_{ej} and the azimuth angle of both the ejected particle ϕ_{ej} and the scattered alpha particle ϕ_s were measured using the silicon detectors. If the ejected particle did not have sufficient energy to be identified as a proton or an alpha particle and this was not determined by other means such as a characteristic gamma, both the mass of ^{20}Ne and ^{23}Na were tried in turn as the mass of the product nucleus m_d. Similarly, the mass of the ejected particle m_{ej} was selected to be that of an alpha particle for the ^{20}Ne case and that of a proton for the ^{23}Na case. The recoil energy of the product nucleus was then determined by conservation of momentum by taking the difference of the ejected particle momentum and the recoil momentum calculated from the scattered alpha particle. The excitation of the product nucleus was then the difference of the excitation of the ^{24}Mg recoil and the kinetic energy of the product nucleus and ejected particle, plus the (negative) Q value for emitting a proton or alpha particle from a ^{24}Mg nucleus.

At higher excitations the proton emitted by ^{24}Mg to create ^{23}Na has enough energy to use the dE-E method of identification. This has been done in Figure 5.19. Using this method,

Nucleus	Excitation Level	Excitation Range	Method
^{20}Ne	Ground State	All	Ejected Particle, no dE-E PID
	1634 keV	All	Ejected Particle, no dE-E PID
	4248 keV	All	2613 keV gamma
	4967 keV	All	3333 keV gamma
	Alpha emitting states	All	Two Ejected Particles
^{23}Na	Ground State	Below 15.5 MeV	Ejected particle, no PID, minus 440 keV state contribution
		Above 15.5 MeV	Ejected proton with dE-E PID, minus 440 keV state contribution
	440 keV	Below 15.5 Me	Ejected particle, no dE-E PID, in coincidence with a 440 keV gamma
		Above 15.5 MeV	Ejected proton, with dE-E PID, in coincidence with a 440 keV gamma
	2076 keV	All	2076 keV gamma minus feeding from 2704 keV level
	2390 keV	All	2390 keV gamma
	2704 keV	All	627 keV gamma
^{23}Mg	Ground	n/a	Not Measured
	450 keV	All	450 keV gamma

Table 5.4: Methods used to measure specific exit channels. All channels were measured in coincidence with a scattered alpha.

the branching ratio for a state was found from the total number of counts in a rectangular gate on Plots 5.17, 5.18, and 5.19. The vertical limits of the gate were placed visually above and below the horizontal band of interest. The horizontal limits were set by the selected excitation bin width of 1 MeV, and each sequential bin was adjacent to the previous bin. The efficiency of detecting the ejected particle was determined using a Monte Carlo simulation. Once an appropriate gate was set, it was also applied to data collected on a carbon target, and this count was scaled and subtracted from the ^{24}Mg target data to account for carbon contamination on the target. The branching ratio for the state and excitation energy slice was then calculated using Equation 5.22. The efficiency for detecting the scattered alpha to determine the ^{24}Mg excitation would appear in both the numerator and denominator and so cancels out.

$$p_{ej} = \sqrt{2m_{ej}E_{ej}} \tag{5.9}$$
$$p_{ej,z} = p_{ej}\cos(\theta_{ej}) \tag{5.10}$$
$$p_{ej,r} = p_{ej}\sin(\theta_{ej}) \tag{5.11}$$
$$p_{ej,x} = p_{ej,r}\cos(\phi_{ej}) \tag{5.12}$$
$$p_{ej,y} = p_{ej,r}\sin(\phi_{ej}) \tag{5.13}$$
$$p_{s,x} = p_{s,r}\cos(\phi_s) \tag{5.14}$$
$$p_{s,y} = p_{s,r}\sin(\phi_s) \tag{5.15}$$
$$p_{d,z} = p_{\text{beam}} - p_{s,z} - p_{ej,z} \tag{5.16}$$
$$p_{d,x} = -p_{s,x} - p_{ej,x} \tag{5.17}$$
$$p_{d,y} = -p_{s,y} - p_{ej,y} \tag{5.18}$$
$$p_d^2 = p_{d,x}^2 + p_{d,y}^2 + p_{d,z}^2 \tag{5.19}$$
$$E_d = \frac{p_d^2}{2m_d} \tag{5.20}$$
$$E_d^* = E_{\text{beam}} - E_s - E_{ej} - E_d + Q_d \tag{5.21}$$

θ_{ej} =Ejected trajectory angle relative to the beam

ϕ_{ej}, ϕ_s =Azimuthal angle around the beam of the ejected particle and the scattered alpha. $\phi = 0$ corresponds to vertically down.

E_{ej} =Kinetic energy of the ejected particle (alpha or proton)

E_d =Kinetic energy of the recoiling product (^{20}Ne or ^{23}Na).

p_{ej} =Momentum of the ejected particle

$p_{ej,z}$ =Ejected particle momentum along the beam line

$p_{ej,r}$ =Ejected particle momentum perpendicular to the beam line

$p_{ej,x}, p_{ej,y}$ =Ejected particle momentum in the vertical and horizontal directions perpendicular to the beam. A positive x value corresponds to down in the experiment.

$p_{s,x}, p_{s,y}$ =Scattered alpha momentum in the vertical and horizontal directions

m_d = Mass of the product. 20*931.5 MeV/c^2 for ^{20}Ne and 23*931.5 MeV/c^2 for ^{23}Na

Q_d = Q value for emitting the ejected particle. -9.31655 MeV for an alpha particle and -11.69269 MeV for a proton.

E_d^* = Corresponding product (^{20}Ne or ^{23}Na) excitation following particle emission.

$$\mathrm{BR} = \frac{N_{\mathrm{gate}}/\eta_{\mathrm{Si}}}{N_{\mathrm{ex}}} \tag{5.22}$$

where:

BR =Branching Ratio

N_{gate} =Net Counts in Gate

η_{Si} =Si Detection Efficiency for Gate

N_{ex} =Total Excited ^{24}Mg in Energy Bin Detected

A second method used a coincidence between the scattered alpha and a characteristic gamma ray of the product ^{20}Ne or ^{23}Na excited state. This works well for states where the feeding of the excited state by gamma deexcitation of higher excited states can be accounted for. In this case the branching ratio is given by Equation 5.23. If higher excitation states of the product nucleus were measured and known to feed a given level, this feeding was subtracted from the gamma counts. The peaks in this method were fitted using a Gaussian function plus a linear function including surrounding channels. Prior to fitting a spectrum

taken from the carbon target was subtracted. Since this spectrum did not have the same peaks, this resulted only in a slight reduction to the background counts and did not have a strong affect on the number of counts attributed to the peak.

$$\mathrm{BR} = \frac{N_{\mathrm{peak}}/\eta_{\mathrm{Ge}}}{N_{\mathrm{ex}}} \tag{5.23}$$

where:

N_{peak} =Net Counts in Gamma Peak
η_{Ge} =Peak Efficiency of the Clover Array for that Gamma

A particle-particle-gamma method was used to separate states that were not clearly separated using the particle method and had sufficient gamma feeding from higher excitation levels to make the scattered alpha-characteristic gamma coincidence alone difficult to correct. The additional coincidence made the separation of the state very specific, but also reduced the available statistics since both the ejected particle detection efficiency and the clover array efficiency had an effect. For this method the gate was set in the same method as the scattered alpha-ejected particle method with the addition of a gate around a characteristic gamma emitted by the excited state of interest. The branching ratio for this method is given by Equation 5.24.

$$\mathrm{BR} = \frac{N_{\mathrm{gate}}/\left(\eta_{\mathrm{Si}} * \eta_{\mathrm{Ge}}\right)}{N_{\mathrm{ex}}} \tag{5.24}$$

Finally, higher excited states of ^{20}Ne decay by alpha decay, which makes the above methods difficult. The Q-value for ^{20}Ne to emit an alpha particle is -4.73 MeV, and the first excited state to primarily decay by alpha emission is at 5.62 MeV. For this and higher states a coincidence between the scattered alpha and two more particle hits was required. The efficiency of the silicon detectors to detect both ejected alpha particles was determined using a Monte Carlo simulation. The result is close to, but not exactly the efficiency for detecting one ejected alpha squared. Part of this deviation is due to separate particle hits in a single sector not being distinguished from each other. This decision was made in order to use the sector detector energy as the particle energy. The other is due to slight differences in the kinematic forward focusing. The branching ratio is determined by Equation 5.25. All alpha emitting states were measured together for each ^{24}Mg excitation slice.

$$\mathrm{BR} = \frac{N_{\mathrm{2ej}}/\eta_{\mathrm{Si,2ej}}}{N_{\mathrm{ex}}} \tag{5.25}$$

where:

N_{2ej} =Number of 2 ejected particle events counted
$\eta_{\mathrm{Si,2ej}}$ =Silicon efficiency to detect two ejected particles

The method used for each state, the gammas used in the gate and whether the ejected particle was required to pass through the dE detector to provide a dE-E particle identification is given in Table 5.4.

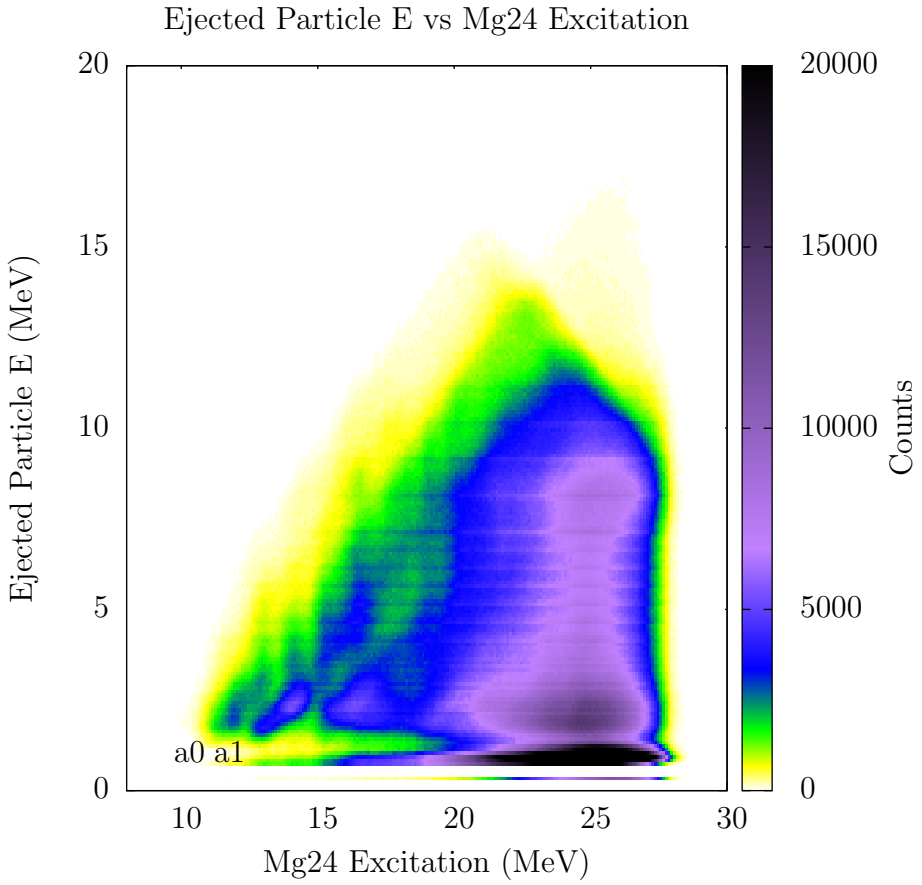

Figure 5.15: The energy of a second particle in coincidence with the scattered alpha. The ejected alpha producing the first excited state of ^{20}Ne intersects the x axis at an excitation of 9.3 MeV and increases with a slope just under 1. Since this slope changes with angle the state is blurred before the ejected angle is accounted for. This second recoil correction is included in Figure 5.17 for alpha channels and 5.18 for proton channels.

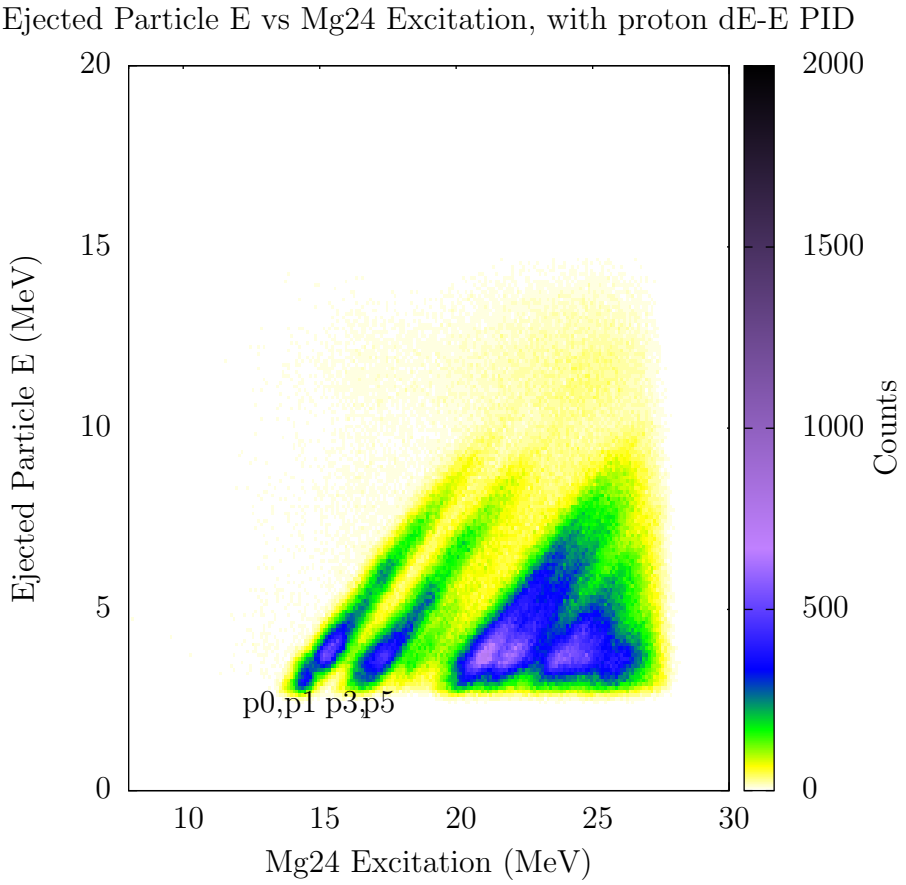

Figure 5.16: The energy of a dE-E identified proton in coincidence with the scattered alpha. Here the excited states of ^{23}Na are more defined in the diagonal lines starting above 11 MeV. The absence of the alpha channels and the lower recoil correction needed by the proton channels results in the cleaner lines. Including the recoil correction results in Figure 5.19.

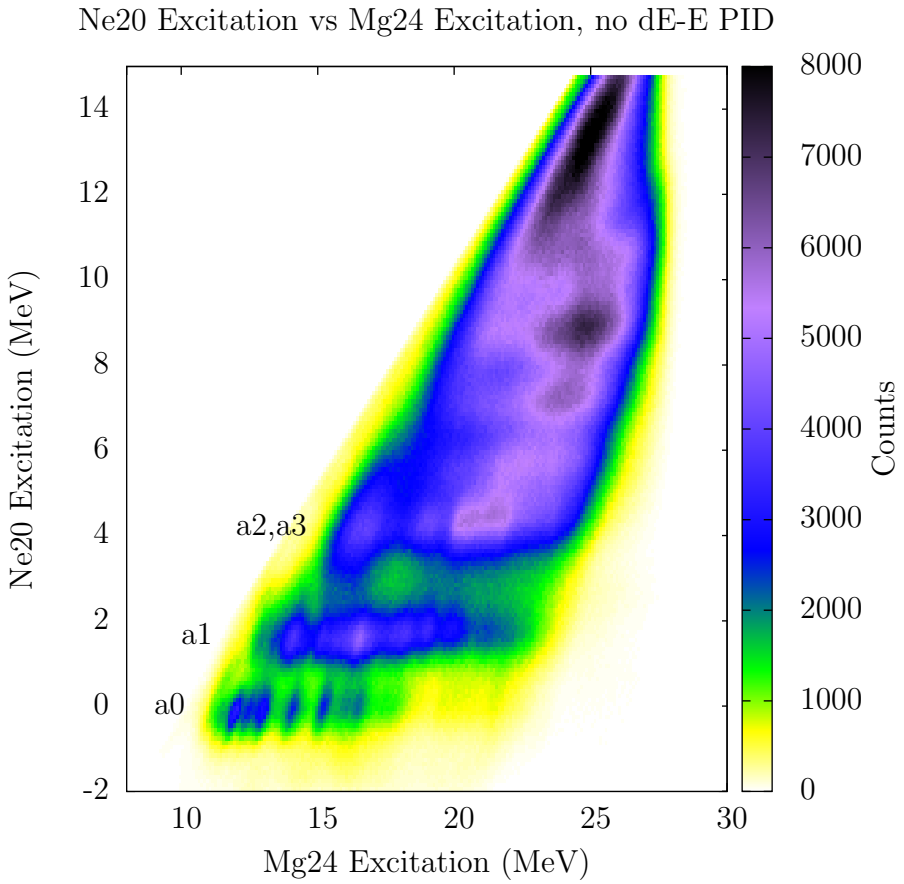

Figure 5.17: The excitation of the ^{20}Ne daughter as a function of the ^{24}Mg excitation found with the scattered alpha. The alpha channels can be seen as horizontal bands.

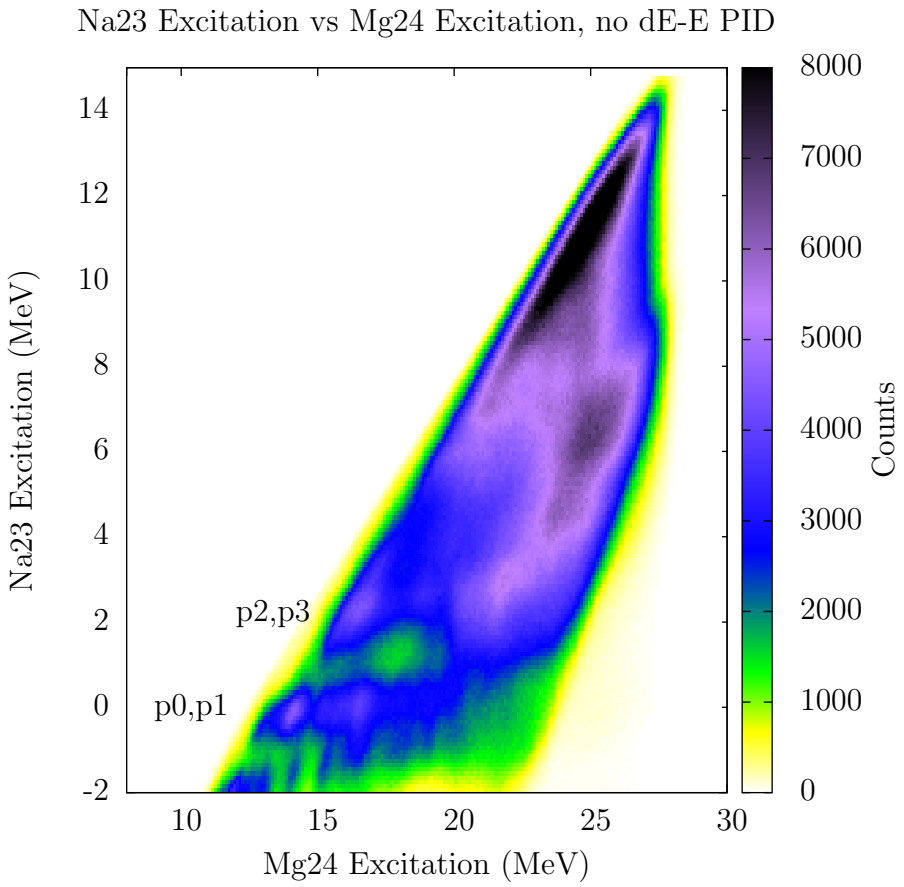

Figure 5.18: The excitation of the ^{23}Na daughter as a function of the ^{24}Mg excitation found with the scattered alpha. No dE-E particle ID was used for the ejected proton. This plot was only used for the range of ^{24}Mg excitation that would lead to a proton with too little energy to pass through the dE detector. The alpha channels leading to ^{20}Ne are visible as slightly sloped horizontal bands.

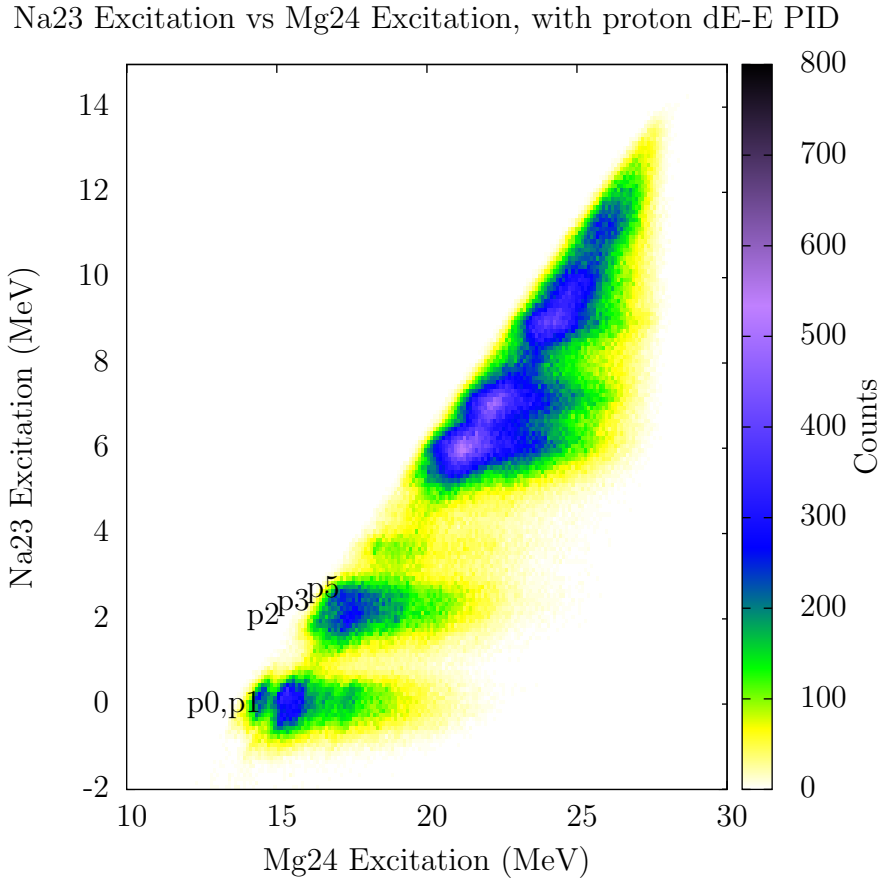

Figure 5.19: The excitation of the ^{23}Na daughter as a function of the ^{24}Mg excitation found with the scattered alpha. A proton dE-E particle ID was required for the ejected proton.

5.5 Resulting Branching Ratios

Comparison of the measured branching ratio to the ground state of ^{20}Ne compares well with the existing measurements for the direct carbon on carbon reaction, as shown in Figure 5.20. This state of ^{20}Ne has a spin and parity of 0^+. The first (1634 keV) and third (4967 keV) excited states, which are 2^+ and 2^- respectively, are both higher than the ^{12}C $+^{12}$ C data, but are within the scatter or error bars, as shown in Figures 5.21 and 5.23. A large deviation is seen for the second excited state (4248 keV) which also has the largest spin of 4^+. In both cases the deviation seems to be shrinking as one moves towards higher excitation energies. The larger branching ratios to higher spin states for inelastically excited ^{24}Mg as compared to ^{12}C $+^{12}$ C causes the total alpha branching ratio to be larger for the inelastic scattering case for the excitation range of 17 MeV to 19 MeV. It is worth noting however that the contribution of the 4^+ state which the largest deviation is small below 16 MeV excitation. It is possible then that the branching ratio around the Gamow window of 15 to 16 MeV is again similar to that for inelastic scattering.

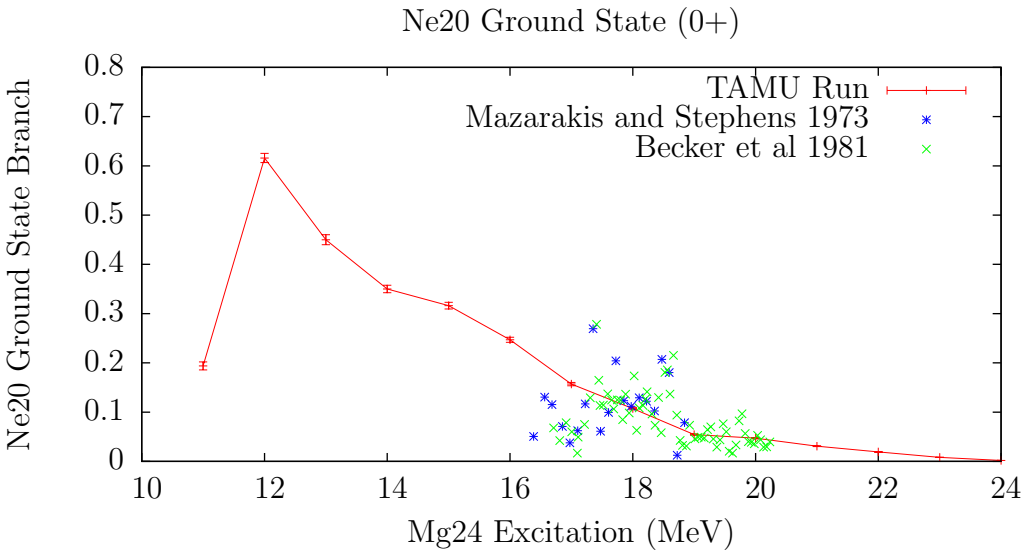

Figure 5.20: Alpha branch to the ground state of ^{20}Ne.

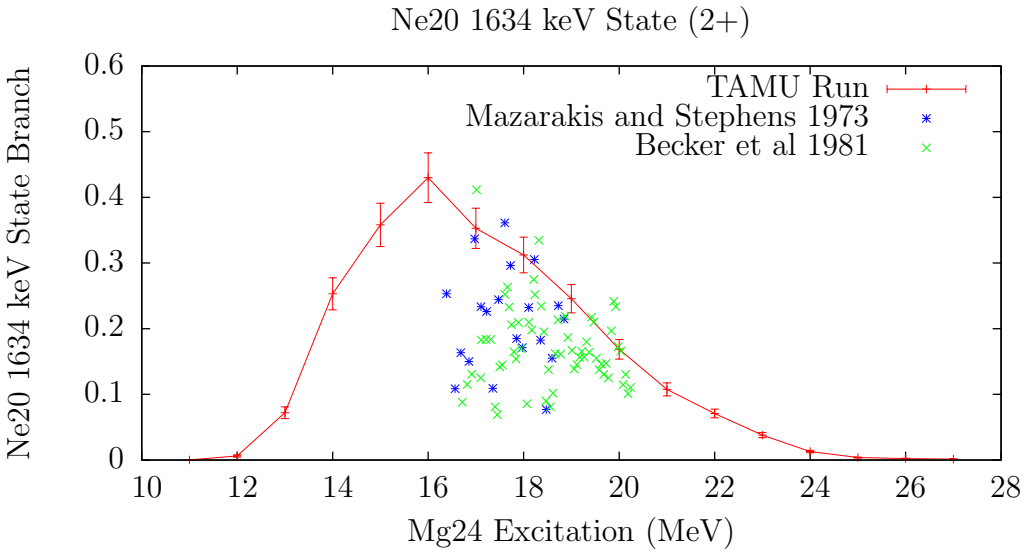

Figure 5.21: Alpha branch to the first excited state of ^{20}Ne.

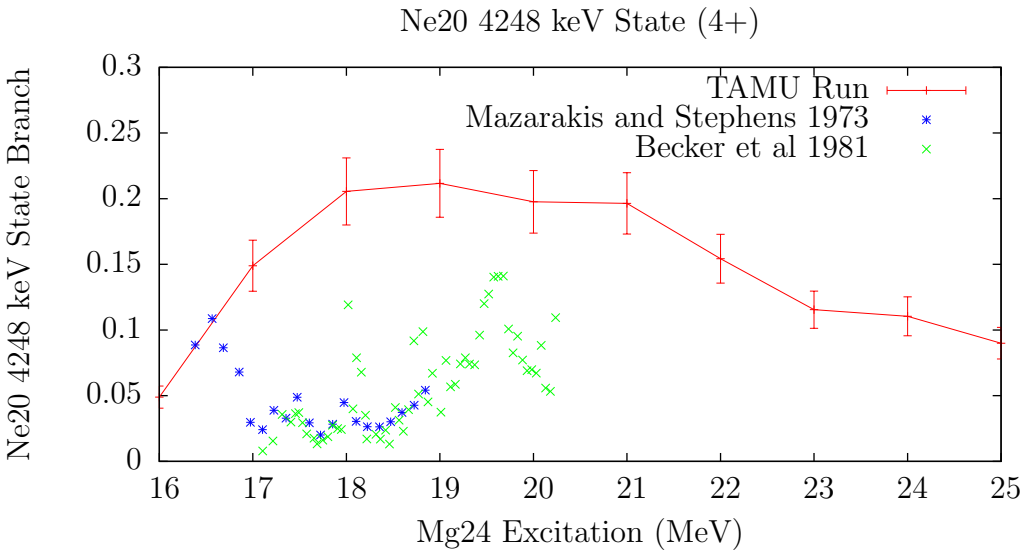

Figure 5.22: Alpha branch to the second excited state of ^{20}Ne.

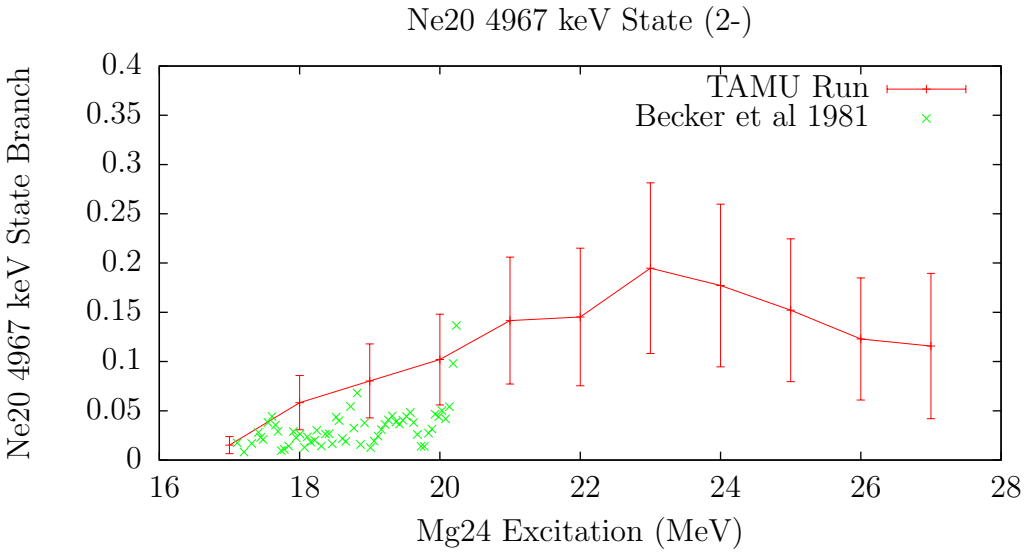

Figure 5.23: Alpha branch to the third excited state of ^{20}Ne.

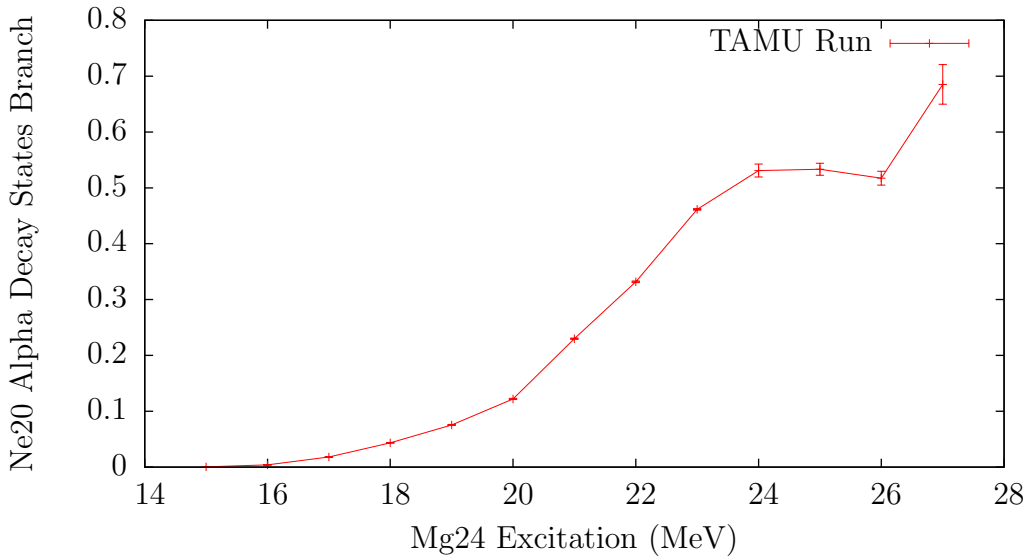

Figure 5.24: Alpha branch to higher excited states of ^{20}Ne which decay by alpha emission.

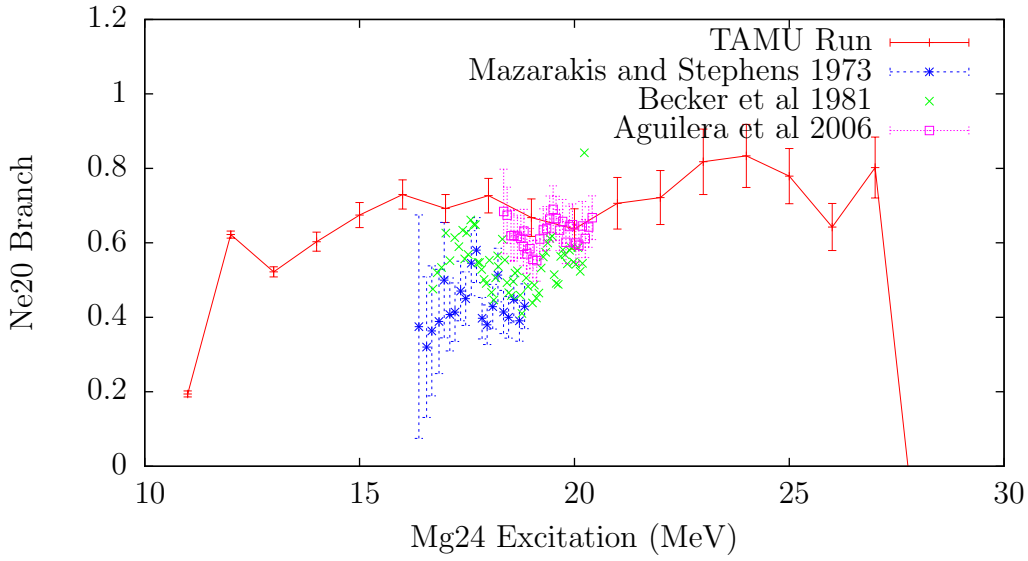

Figure 5.25: Total alpha branch (ground plus all excited states of ^{20}Ne). This includes excited states of ^{20}Ne which decay by alpha emission. The reference data is from [1], [3], and [5].

Comparisons of the current inelastic scattering data to the existing $^{12}C + ^{12}C$ data also shows that the current inelastic scattering experiment favors states with higher spin as compared to $^{12}C + ^{12}C$ reactions. Here the best agreement seems to be with the 2076 keV 7/2+ state (Figure 5.28, with states of lower spin having branching ratios smaller than that for $^{12}C + ^{12}C$ and the 2704 keV 9/2+ state having a slightly higher branching ratio than for $^{12}C + ^{12}C$ reactions.

The fourth excited state of ^{23}Na was not observed, and in the $^{12}C + ^{12}C$ data the fourth and fifth states were not resolved from each other. In Figure 5.30 the sum of the fourth and fifth states is compared to the current measurement for the fifth state alone.

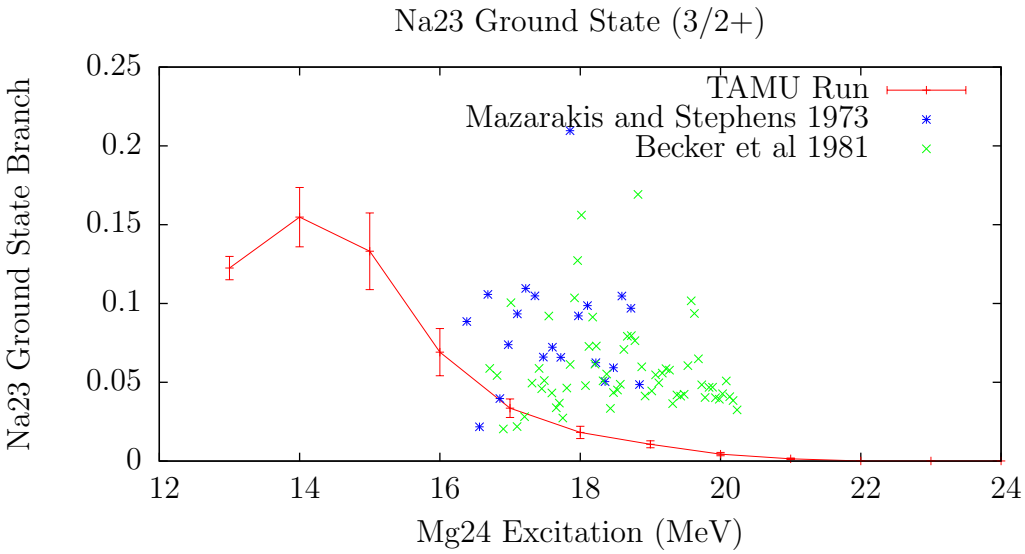

Figure 5.26: Proton branch to the ground state of ^{23}Na

;

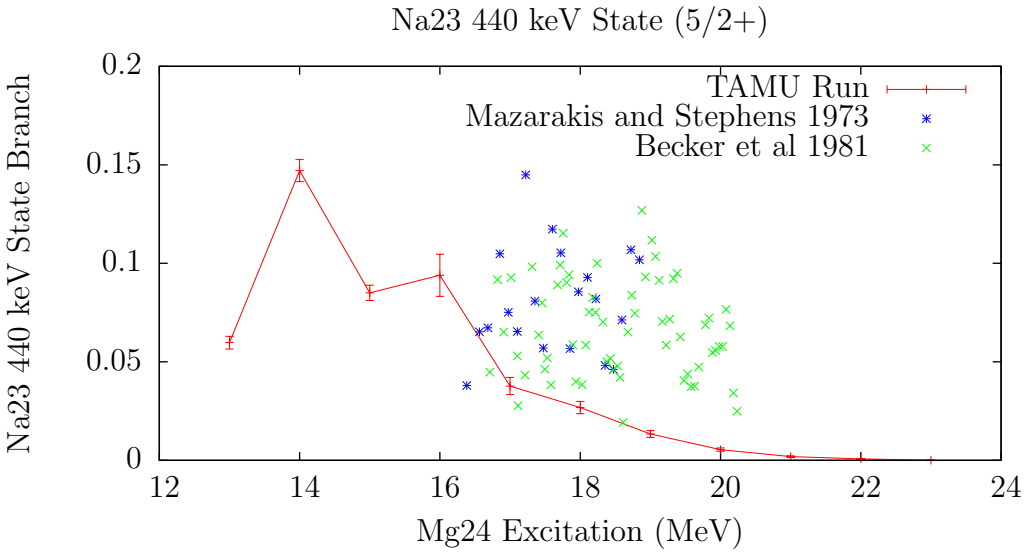

Figure 5.27: Proton branch to the first excited state of ^{23}Na

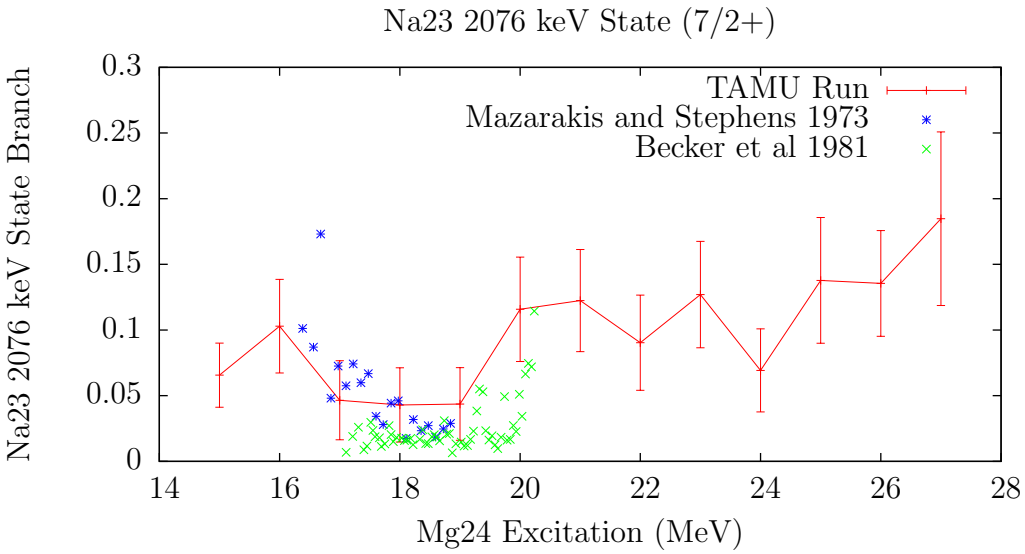

Figure 5.28: Proton branch to the second excited state of ^{23}Na

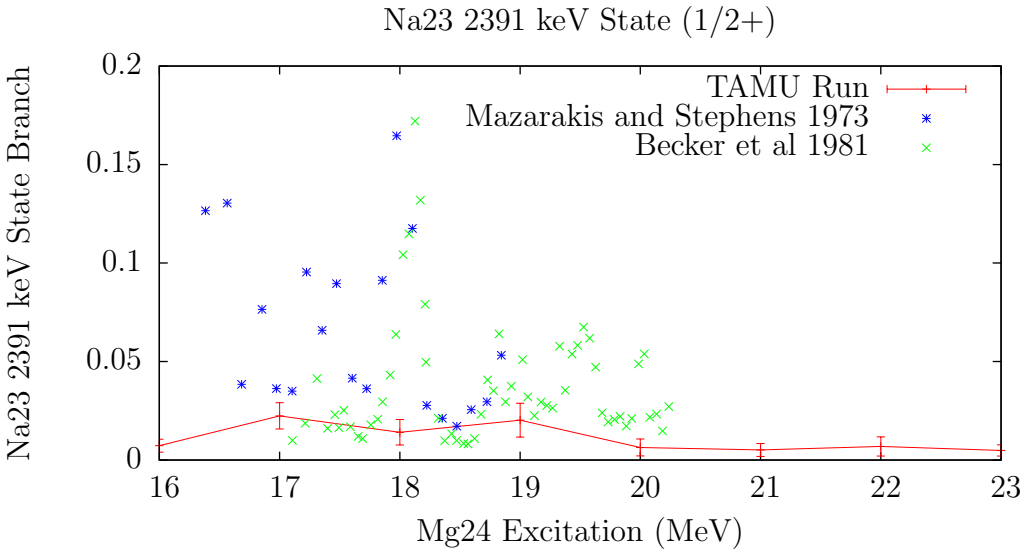

Figure 5.29: Proton branch to the third excited state of ^{23}Na

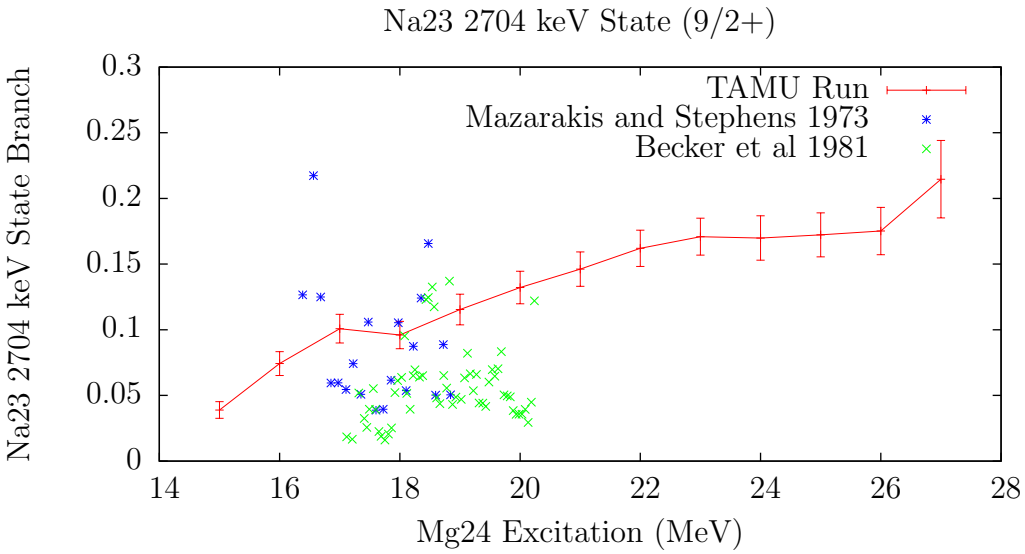

Figure 5.30: Proton branch to the fifth excited state of ^{23}Na. Gamma rays from the fourth excited state were not seen. Comparison data is for the fourth and fifth excited states combined, which were not resolved.

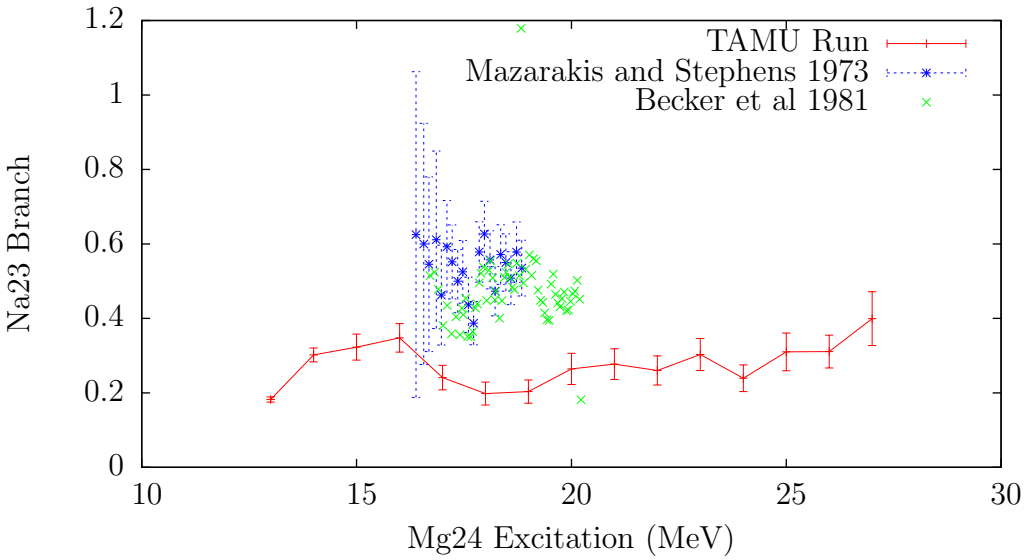

Figure 5.31: Total proton branch (ground plus all excited states of ^{23}Na)

The ground state branch for ^{23}Mg could not be measured in the current setup since the emitted particle is a neutron and not a charged particle, and no neutron detectors were present. The first excited state was measured using the 451 keV gamma ray. No estimate for the ground state contribution was attempted. This is expected to have a small effect at higher excitation energies starting around 17 MeV, but is not a factor at excitation energies in the Gamow window of 15 to 16 MeV.

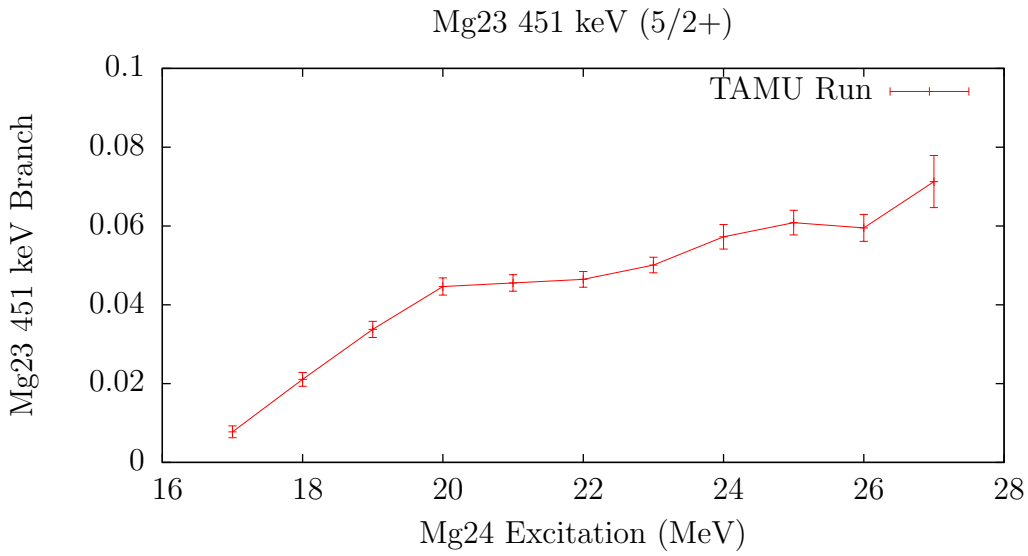

Figure 5.32: Neutron branching ratio to the first excited state of ^{23}Mg. Higher excitation states were not measured, and gamma cascading from these levels may be included at higher excitations. This is not expected to be an issue at energies relevant to the Gamow window.

5.6 Efficiency Check

By definition, the sum of the branching ratios of all exit channels sum to one. Therefore the sum of all the branching ratio measurements should also sum to one. In this way summing the measured branching ratios is a check for the measurement. A sum that does not equal one can indicate that the counting efficiency is not known well enough, that some channels are missing, or that the number of counts for some channels includes events not actually belonging to that channel.

The main channel which is not shown in Section 5.4 is the emission of gamma rays by ^{24}Mg. This is not a major factor at the excitation energies relevant to carbon burning, but is important at slightly lower excitation energies below the point where particle emission channels open up. Many states in ^{24}Mg which gamma decay often do so through the first excited state at 1369 keV. Because of this, most of the gamma branch can be measured by measuring this single gamma energy. The 4237 keV gamma offers one of the paths that bypasses the 1369 keV state. Other gamma transitions which bypass both of these states are at energies greater than 5 MeV. The upper energy range for the gamma detectors was between 5 and 6 MeV depending on the specific detector and segment within the detector. Thus the gamma decay channel for ^{24}Mg is mostly but not completely captured.

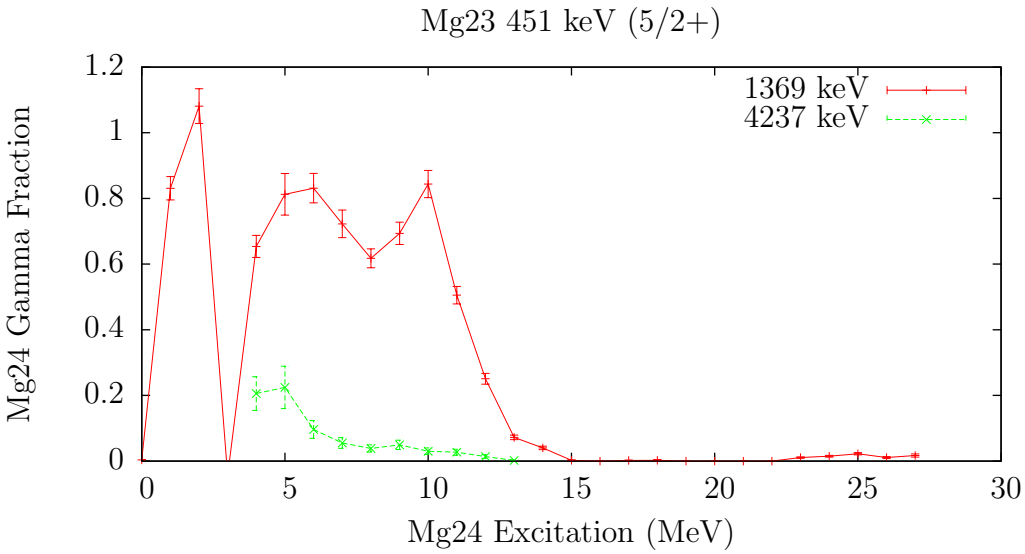

Figure 5.33: Gamma rays emitted at 1369 keV and 4237 keV per ^{24}Mg excitation. The dip near 3 MeV is due to the absence of any state in ^{24}Mg

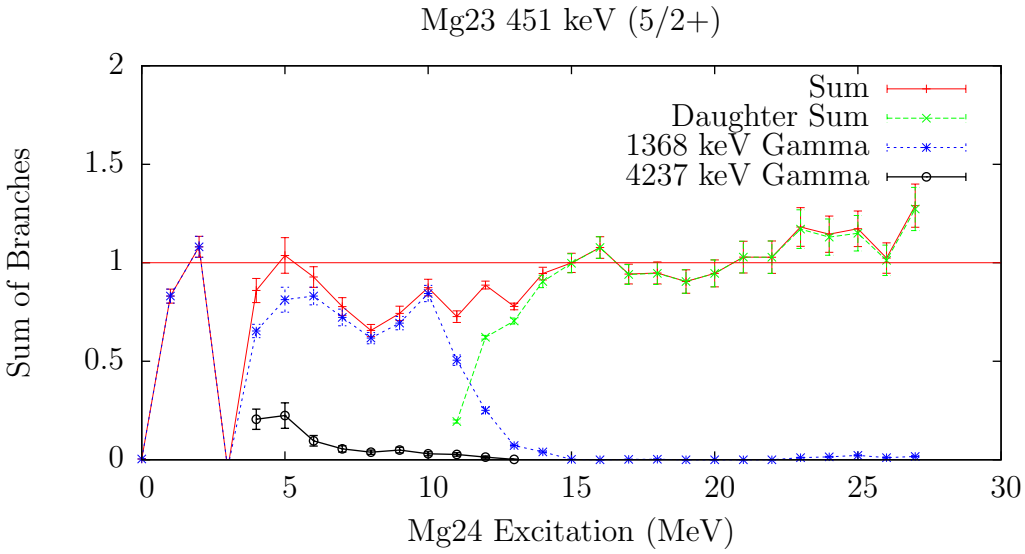

Figure 5.34: The sum of the measured gamma, alpha, proton, and neutron channels. Note that in the energy range applicable to carbon burning (14 to 17 MeV) the sum is nearly one.

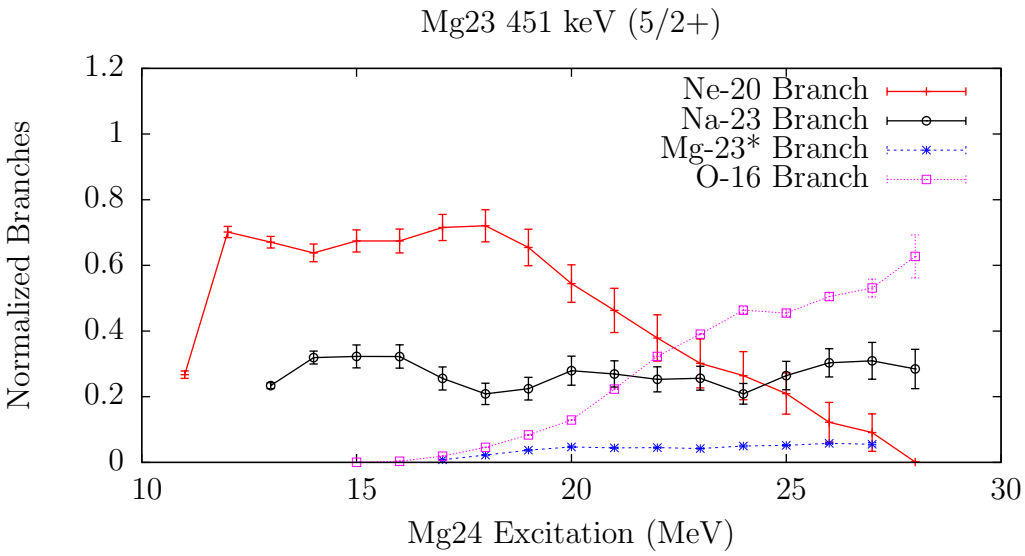

Figure 5.35: Total branching ratios for the alpha, proton, and neutron channels. The ratios are normalized by setting the total of all branches shown in Figure 5.34 to one for all energies. No ground state contribution was assumed for the neutron channel. For equivalent ^{12}C +^{12} C center of mass energies subtract 13.934 from the ^{24}Mg excitation energy.

5.7 Normalized Branching Ratios

The final total branching ratios, shown in Figure 5.35 have been normalized using the sum in Figure 5.34 such that the sum of all branching ratios is 1. Since higher excited states of ^{20}Ne decay by alpha particle emission, these states are not included in the total for ^{20}Ne and are instead shown separately under the label ^{16}O, the resulting nucleus after ^{20}Ne emits an alpha particle. The total alpha branch is the sum of the branch leaving ^{20}Ne and the branch leaving ^{16}O as the product nucleus. This distinction only applies at higher excitation energies and not in the excitation energy range corresponding to the Gamow window for carbon burning.

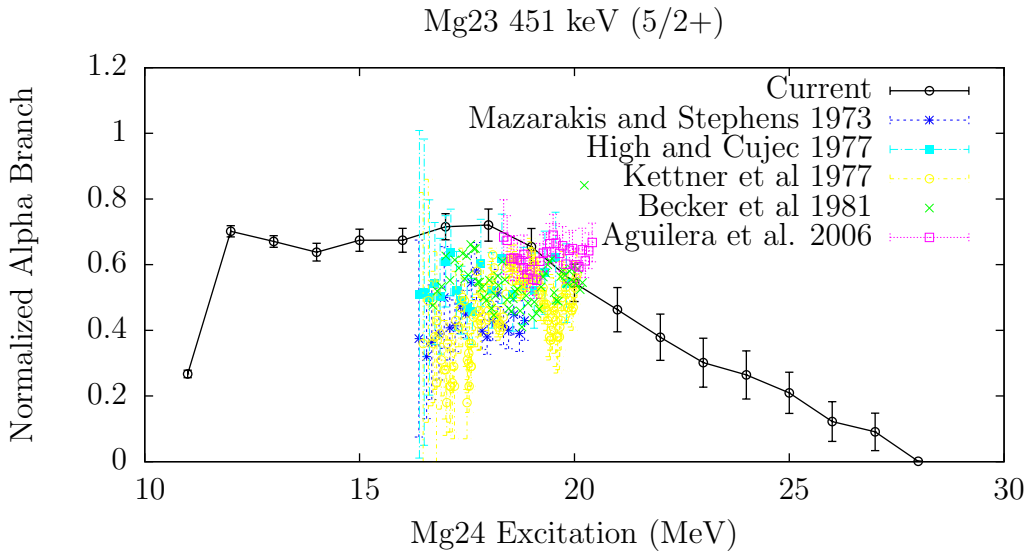

Figure 5.36: Total branching ratio for the formation of ^{20}Ne and a comparison to the previous measurements in [1], [5], [36], and [37]. Higher excited states of ^{20}Ne that decay by alpha emission and form ^{16}O are not included here.

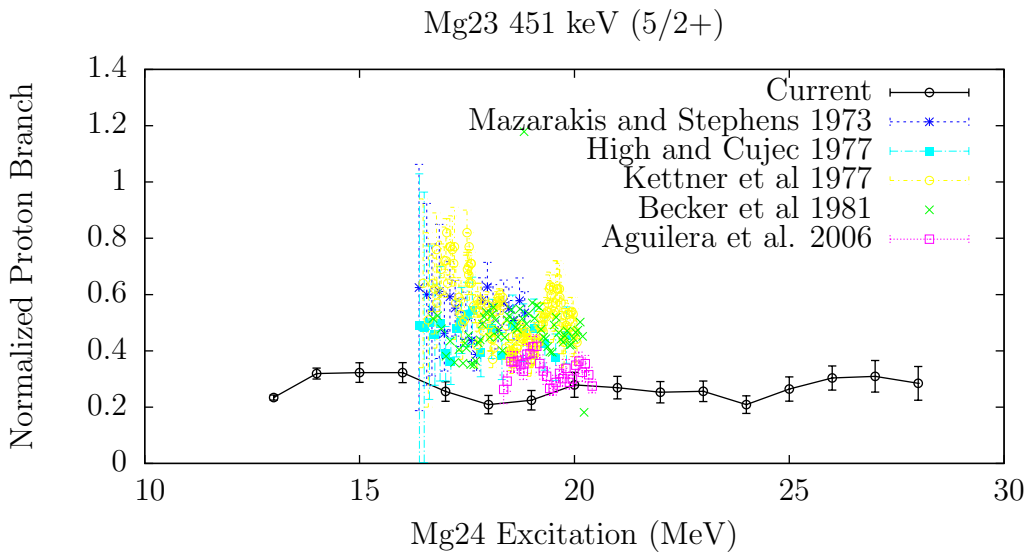

Figure 5.37: Total ^{23}Na branching ratio and a comparison to the previous measurements in [1], [5], [36], and [37]. The data for the 1977 measurement by High and Čujic is the sum of the proton and neutron branches and is therefore greater than the proton branch alone at excitation energies with a measurable neutron branch.

Chapter 6

Conclusion

Measurements of the branching ratios for the decay of ^{24}Mg excited by the inelastic scattering of 40 MeV alpha particles have been made. The range of excitation energies studied extends to 27 MeV. This range includes the excitation energies present in the ^{24}Mg compound nucleus formed in carbon burning reactions, which have excitation energies in the range of 15 to 16 MeV. This experiment was selected as a possible surrogate measurement for the branching ratios for the carbon burning compound nucleus, and consequently the ratios of the cross sections for the reactions $^{12}\mathrm{C} + ^{12}\mathrm{C} \rightarrow ^{20}\mathrm{Ne} + \alpha$, $^{12}\mathrm{C} + ^{12}\mathrm{C} \rightarrow ^{23}\mathrm{Na} + \mathrm{p}$, and $^{12}\mathrm{C} + ^{12}\mathrm{C} \rightarrow ^{23}\mathrm{Mg} + \mathrm{n}$.

The angular distribution of the scattered alpha particles leading to ^{24}Mg excitation energies similar to those present in a carbon burning reaction compound nucleus show some preference for smaller angles in the region of 0.4 to 0.8 radians. A fully compound reaction mechanism for inelastic scattering would produce an angular cross section that is approximately isotropic. This indicates that the scattering mechanism is not only that of a compound reaction. Scattering in a compound reaction would leave the nucleus in a state that is similar to the compound nucleus in a carbon burning reaction but this does not rule out the possibility that a nucleus excited by a different mechanism would evolve into a state similar to that of a carbon burning compound nucleus.

A related issue is that of the angular momentum distribution of the inelastically excited ^{24}Mg as compared to the ^{24}Mg compound nucleus in carbon burning. Inelastic scattering of 40 MeV alpha particles has the potential to bring in higher amounts of angular momentum than expected for the carbon burning compound nucleus. If the Weisskopf-Ewing limit holds for this system then the difference in the angular momentum distributions will not affect the branching ratios, but this assumption must be supported by comparisons to data taken from direct carbon on carbon experiments. These comparisons show that at least for certain ranges of excitation energy that inelastic scattering of 40 MeV alpha particles produces a distribution of excited ^{24}Mg that favors decays into higher spin states of ^{20}Ne and ^{23}Na relative to the excited ^{24}Mg created as the compound nucleus in carbon burning. This indicates that this system does not fully meet the criteria for the Weisskopf-Ewing limit. It

also suggests that the average spin distribution in the inelastically excited ^{24}Mg is higher than that of the ^{24}Mg compound nucleus in carbon burning.

While these differences prevent assigning a direct equality between the branching ratios found with inelastic scattering and in carbon burning, the branching ratios found in the inelastic scattering case do appear to have a relation to those in carbon burning which might allow an estimate of the branching ratios for carbon burning to be made in the region of the Gamow window. The branching ratios to some states of ^{20}Ne and ^{23}Na were very similar for the inelastic scattering case and the carbon burning case. Additionally, as the excitation energy is decreased to the range of the Gamow window many of the branching ratios to the higher excited states diminish, reducing the total number of states which must be understood in order to predict the branching ratio.

Bibliography

[1] M. G. Mazarakis and W. E. Stephens. Experimental measurements of the ^{12}C +^{12} C nuclear reactions at low energies. *Physical Review C*, 7(4):1280–1287, 1973.

[2] R. Dayras, Z. E. Switkowski, and S. E. Woosley. Neutron branching in the reaction 12c + 12c. *Nuclear Physics A*, 279(1):70–84, 1977.

[3] H.W. Becker, K.U. Kettner, C. Rolfs, and H.P. Trautvetter. The12c+12c reaction at subcoulomb energies (ii). *Zeitschrift fÃ¼r Physik A Atoms and Nuclei*, 303(4):305–312, 1981.

[4] L. Barrón-Palos, E. Chávez L., A. Huerta H., M. Ortiz, G. Murillo O., E. Aguilera R., E. Martınez Q., E. Moreno, R. Policroniades R., and A. Varela G. ^{12}C +^{12} C cross-section measurements at low energies. *The European Physical Journal A - Hadrons and Nuclei*, 25:645–646, 2005. 10.1140/epjad/i2005-06-008-2.

[5] E. F. Aguilera, P. Rosales, E. Martinez-Quiroz, G. Murillo, M. Fernández, H. Berdejo, D. Lizcano, A. Gómez-Camacho, R. Policroniades, A. Varela, E. Moreno, E. Chávez, M. E. Ortíz, A. Huerta, T. Belyaeva, and M. Wiescher. New [gamma]-ray measurements for ^{12}c + ^{12}c sub-coulomb fusion: Toward data unification. *Physical Review C*, 73:064601, 2006.

[6] L. Barrón-Palos, E.F. Aguilera, J. Aspiazu, A. Huerta, E. Martínez-Quiroz, R. Monroy, E. Moreno, G. Murillo, M.E. Ortiz, R. Policroniades, A. Varela, and E. Chávez. Absolute cross sections measurement for the 12c + 12c system at astrophysically relevant energies. *Nuclear Physics A*, 779:318–332, 2006.

[7] T. Spillane, F. Raiola, C. Rolfs, D. Schürmann, F. Strieder, S. Zeng, H.-W. Becker, C. Bordeanu, L. Gialanella, M. Romano, and J. Schweitzer. ^{12}C +^{12} C fusion reactions near the gamow energy. *Physical Review Letters*, 98:122501, 2007.

[8] Claus E. Rolfs and William S. Rodney. *Cauldrons in the Cosmos*. The University of Chicago Press, Chicago 60637, 1988.

[9] C. J. Hansen and S. D. Kawaler. *Stellar Interiors: Physical Principles, Structure, and Evolution*. Springer-Verlag New York, Inc., 1994.

[10] Q value calculator. http://www.nndc.bnl.gov/qcalc/. Accessed: 2015-04-19.

[11] Jutta E. Escher, Frank S. Dietrich, and Christian Forssén. Surrogate nuclear reaction methods for astrophysics. *Nuclear Instruments and Methods in Physics Research Section B: Beam Interactions with Materials and Atoms*, 261(1-2):1075–1078, 2007. The Application of Accelerators in Research and Industry - Proceedings of the Nineteenth International Conference on The Application of Accelerators in Research and Industry, Nineteenth International Conference on The Application of Accelerators in Research and Industry.

[12] K. Lundmark. *Svenska Vetenkapsakad. Handl.*, 60:8, 1920.

[13] Wolfgang Hillebrandt and Jens C. Niemeyer. Type ia supernova explosion models. *Annual Review of Astronomy and Astrophysics*, 38:191 – 230, 2000.

[14] W. Baade and F. Zwicky. Remarks on super-novae and cosmic rays. *Phys. Rev.*, 46(1):76–77, Jul 1934.

[15] R. Minkowski. *Publ. Astron. Soc. Pac.*, 52:206, 1940.

[16] J. C. Wheeler and R. P. Harkness. *Rep. Prog. Phys.*, 53:1467–557, 1990.

[17] F. Hoyle and W. A. Fowler. Nucleosynthesis in supernovae. *Astrophysical Journal*, 132:565–590, 1960.

[18] J. W. Truran, D. Arnett, and A. G. W. Cameron. *Canad. J. Physics*, 45:2315–32, 1967.

[19] S. A. Colgate and C. McKee. *Astrophysical Journal*, 157:623, 1969.

[20] F. Zwicky. On the theory and observation of highly collapsed stars. *Phys. Rev.*, 55(8):726–743, Apr 1939.

[21] O. C. Wilson. *Astrophysical Journal*, 90:634, 1939.

[22] F. Hoyle. The synthesis of elements from hydrogen. *M. N. R. A. S.*, 106:343 – 383, 1946.

[23] C. Marty. Generalized optical theorem and integrated cross-sections. *Zeitschrift für Physik A Hadrons and Nuclei*, 309:261–265, 1983. 10.1007/BF01413758.

[24] R. and Lipperheide. Heavy-ion reaction cross sections from elastic scattering data. *Nuclear Physics A*, 469(1):190–204, 1987.

[25] A. N. Ostrowski, T. Davinson, K. Föhl, M. Seidl, and H. Voit. Carbon-burning: Total reaction cross section at ec.m.=2.5-1.6 mev. *Nuclear Physics A*, 688(1-2):130–133, 2001.

[26] C. L. Jiang, K. E. Rehm, B. B. Back, and R. V. F. Janssens. Expectations for ^{12}C and ^{16}O induced fusion cross sections at energies of astrophysical interest. *Physical Review C*, 75:015803, 2007.

[27] R. Bass. Fusion of heavy nuclei in a classical model. *Nuclear Physics A*, 231:45 – 63, 1974.

[28] R. Bass. Nucleus-nucleus potential deduced from experimental fusion cross sections. *Physical Review Letters*, 39(5):265 – 268, 1977.

[29] Nndc website. http://www.nndc.bnl.gov/. Accessed: 2015-06-15.

[30] Frank S. Dietrich. Simple derivation of the hauser-feshbach and weisskoph-ewing formulae, with application to surrogate reactions ucrl-tr-201718.

[31] Jutta E. Escher and Frank S. Dietrich. Determining (n, f) cross sections for actinide nuclei indirectly: Examination of the surrogate ratio method. *Phys. Rev. C*, 74:054601, Nov 2006.

[32] A. J. Koning, S. Hilaire, and M. C. Duijvestijn. Talys-1.0. *Proceedings of the International Conference on Nuclear Data for Science and Technology - ND2007*, pages 211 – 214, 2007.

[33] S.R. Lesher, L. Phair, L.A. Bernstein, D.L. Bleuel, J.T. Burke, J.A. Church, P. Fallon, J. Gibelin, N.D. Scielzo, and M. Wiedeking. Stars/liberace: Segmented silicon and high-purity germanium detector arrays for low-energy nuclear reaction and structure studies. *Nuclear Instruments and Methods in Physics Research Section A: Accelerators, Spectrometers, Detectors and Associated Equipment*, 621(1â€“3):286 – 291, 2010.

[34] M. Pignanelli, S. Micheletti, R. De Leo, S. Brandenburg, and M. N. Harakeh. Nuclear matter density effects in monopole transitions. *Phys. Rev. C*, 33:40–49, Jan 1986.

[35] Kenneth S. Krane. *Introductory Nuclear Physics*. John Wiley & Sons, Inc., 1988.

[36] M.D. High and B. ÄŒujec. The 12c + 12c sub-coulomb fusion cross section. *Nuclear Physics A*, 282(1):181 – 188, 1977.

[37] K. U. Kettner, H. Lorenz-Wirzba, C. Rolfs, and H. Winkler. Study of the fusion reaction ^{12}C + ^{12}C below the coulomb barrier. *Phys. Rev. Lett.*, 38:337–340, Feb 1977.